Atmos. Chem. Phys. Discuss., 11, 16499–16552, 2011
www.atmos-chem-phys-discuss.net/11/16499/2011/
doi:10.5194/acpd-11-16499-2011

Atmospheric Chemistry and Physics Discussions

ARCTAS-A ground-based observational campaign and meteorological context, interior Alaska, April 2008

D. E. Atkinson[1,2,*], **K. Sassen**[2,3], **M. Hayashi**[4], **C. F. Cahill**[3,6], **G. Shaw**[3,5], **D. Harrigan**[7], **and H. Fuelberg**[7]

[1]International Arctic Research Center, University of Alaska Fairbanks, 930 Koyukuk Drive, Fairbanks, Alaska, 99775, USA
[2]Department of Atmospheric Sciences, University of Alaska Fairbanks, 930 Koyukuk Drive, Fairbanks, Alaska, 99775, USA
[3]Geophysical Institute, University of Alaska Fairbanks, 903 Koyukuk Drive, Fairbanks, Alaska, 99775, USA
[4]Department of Earth System Science, University of Fukuoka, 8-19-1 Nanakuma, Jonan-ku, Fukuoka, 814-0180, Japan
[5]Department of Physics, University of Alaska Fairbanks, P.O. Box 755920, Fairbanks, AK 99775-5920, USA
[6]Department of Chemistry, University of Alaska Fairbanks, P.O. Box 755920, Fairbanks, AK 99775-5920, USA

[7]Department of Meteorology, The Florida State University, Department of Meteorology/ 404 LOV, 1017 Academic Way/P.O. Box 3064520, Tallahassee, FL 32306-4520, USA
[*]Present address: Department of Geography, University of Victoria, P.O. Box 3060 STN CSC, Victoria, BC, V8W 3R4, Canada

Received: 20 April 2011 – Accepted: 24 April 2011 – Published: 10 June 2011

Correspondence to: D. E. Atkinson (datkinso@uvic.ca)

Published by Copernicus Publications on behalf of the European Geosciences Union.

ACPD
11, 16499–16552, 2011

Abstract

Arctic aerosol loading in interior Alaska displays a strong seasonality, with pristine conditions generally prevailing during winter months and increasing frequency of midlatitude air intrusions occurring in spring. By summer, local aerosol sources, like boreal forest fire smoke, may come into prominence. Long term aerosol research from the University of Alaska Fairbanks indicates that the period around April typically marks the beginning of the retreat of the Polar Front, opening the free exchange of midlatitude air. In April 2008 the NASA ARCTAS field campaign was conducted, supported in Fairbanks by comprehensive polarization (0.693 µm) lidar, surface and balloon-borne aerosol measurements, and synoptic weather analyzes. The data provided information on the vertical distribution and type of aerosol, the size distributions and chemical nature of the surface aerosol, as well as the large scale view of aerosol transport conditions to Alaska. We found evidence to suggest four major aerosol loading events in the 25 March–30 April 2008 timeframe: a typical Arctic haze event, several days of extremely clear conditions, rapid onset of a period dominated by Asian dust with some smoke, and a period dominated by Asian smoke. A focused case study analysis conducted on 19 April 2008 using a balloon-borne optical particle counter suggested that, on this day, the majority of the suspended particulate matter consisted of Asian dust although a contribution from Asian smoke cannot be ruled out on the basis of backtrack analysis. In the last week of April concentrations gradually decreased as synoptic conditions shifted away from favoring transport to Alaska.

1 Introduction

In April 2008 the NASA project, "Arctic Research of the Composition of the Troposphere from Aircraft and Satellites" (ARCTAS), was conducted over Alaska and its marginal seas. This effort had several objectives, one of which was to examine long-range transport of pollutants to the Arctic (Jacob et al., 2010) during the traditional

ACPD
11, 16499–16552, 2011

period of maximum concentrations of distal industrial pollutants over the region, what is termed “arctic haze” (Shaw, 1995), with a broader objective of placing this in the context of radiative forcing and climate change. To provide the greatest potential for capturing haze events project timing was correspondingly set to the mid-spring period. To achieve its objective, the project oversaw an intensive series of aircraft- and ground-based observations of atmospheric chemistry state. Jacob et al. (2010) discuss in detail the overall project rationale, design, discharge, and some major results. This paper focuses on the meteorological context of the ground-based component of the first phase of the mission, ARCTAS-A, and does not consider the June/July phase, conducted over northern Alberta.

At several locations in the Alaska Interior (Fig. 1) a suite of ground-based in situ and remotely-sensed observations were gathered during the ARCTAS-A experiment. These included several forms of direct aerosol sampling, both ground-based and balloon-launched, as well as remotely sensed data acquired by ground-based lidar and sun photometry instruments. Each provided different information – chemical species, particle size, nature, and quantity – that contributed to an overall picture of the nature of transport to this area. For this paper the lidar and airborne particle size data will be considered in greatest detail. A closer examination of the other parameters – directly measured microphysical and chemical aspects of the ground-based campaign – are being treated in companion papers; only broad overviews of ground-based chemical and particulate results are employed here to help frame major time periods of interest.

In support of ARCTAS-A Fuelberg et al. (2010) have provided a broad meteorological overview of the northern hemisphere from the Arctic down to the mid-latitudes. They briefly reviewed the climatological context and indicated how the 30 March to 22 April 2008 period differed from climatology and they provided a comprehensive assessment of mean atmospheric state during the mission timeframe. The synoptic objective of this paper is to build upon the results of Fuelberg et al. by focusing in on the Alaska Interior and investigating the meteorological context that explains the results from the ground- and balloon-based observations, with particular focus on identifying

ACPD
11, 16499–16552, 2011

relative loading contributions from smoke vs crustal/mineral sources. To do this two tasks are undertaken:

1. Identify the major epochs of atmospheric aerosol state over Interior Alaska as manifested in the data obtained by the ground-based instrumental array.

2. Examine the meteorological controls in place during the identified aerosol epochs that governed episodes of long-range aerosol transport into the region. Particular focus will be given to a case-study day during which direct sampling of the vertical column was conducted.

2 Data and methods

2.1 Meteorological data and analysis methods

Data to perform the meteorological assessments were drawn from the reanalysis datasets held at NOAA's Earth System Research Laboratory and include the NCEP/NCAR Global reanalysis (NNR) dataset (Kalnay et al., 1996), developed at NOAA's National Centers for Environmental Prediction in conjunction with the National Center for Atmosphere Research (NCEP/NCAR). The NNR dataset possesses a spatial resolution of 2.5° latitude and longitude, temporal resolution of 6 h, and is useful for establishing broad features of the large scale flow and, in particular, anomaly patterns.

The reanalysis data were used to identify general patterns in flow to explain the ground-based observations. The extent to which patterns were typical or anomalous is also discussed. Parameters utilized for large-scale examinations consisted mostly of geopotential height, typically mid- to low-troposphere pressure levels were used to categorize flow; wind data and temperature were mentioned where useful. To assist in source-region interpretation and attribution, selected trajectory analyses were conducted by Harrison and Fuelberg using the FLEXPART dispersion model system as applied to their northern-hemisphere WRF data (Fuelberg et al., 2010).

ACPD
11, 16499–16552, 2011

2.2 Ground-based observations

The ground-based observationa array consisted of a series of instruments situated at various locations in the Alaska Interior (Fig. 1), centered in Fairbanks and just north of town, at the Poker Flat Research Range. The primary ground-based observations used in this study were obtained from a DRUM impact sampler, which guided the framing of major periods aerosol loading epochs, and from a series of near-daily polarization lidar shots, which guided assessment of broad aerosol type aloft. Supporting data came from a Scanning Mobility Particle Spectrometer. A focused case-study was performed for one day (19 April) with the aid of vertical in-situ sampling using a balloon-borne optical particle counter. These systems are described below.

2.2.1 Arctic Facility for Atmospheric Remote Sensing (AFARS)

The Arctic Facility for Atmospheric Remote Sensing (AFARS) is located on the University of Alaska Fairbanks campus (64.86° N and −147.84° W, at 286 m a.m.s.l., above mean sea level). At this facility is operated a "turnkey" Cloud Polarization Lidar (CPL) system and a 3.2 mm W-band radar (not used in this project), in operation since early 2004. The CPL is able to take polarization measurements at 0.532, 0.694, and 1.06 lidar wavelengths. A delay in servicing meant the laser output was reduced by about a factor of two to three, necessitating increased averaging times to compute reliable depolarization data. CPL linear depolarization ratios (see below) are accurate to about ±0.02 for the range of aerosol values repeated here.

To obtain depolarization measurements of the backscatter from linearly-polarized transmitted laser light, the linear depolarization ratio is computed from the ratio of the backscattered laser powers in two of the orthogonal polarization planes relative to that transmitted, as a function of range (R). For simple two-channel polarization lidars, the "total" linear depolarization ratio is defined by

ACPD
11, 16499–16552, 2011

$$\delta = \frac{P(R)_{\perp}}{P(R)_{\parallel}} = \frac{\left[\beta_{\mathrm{m}}(R)_{\perp} + \beta_{\mathrm{a}}(R)_{\perp} + \beta_{\mathrm{c}}(R)_{\perp}\right]}{\left[\beta_{\mathrm{m}}(R)_{\parallel} + \beta_{\mathrm{a}}(R)_{\parallel} + \beta_{\mathrm{c}}(R)_{\parallel}\right]} \quad (1)$$

where the subscripts m = molecular, a = aerosol, and c = cloud represent the contributions to backscattering from each species category. Although the relatively strong backscattering from clouds tends to dominate the total signal, a mixture of molecules and aerosols can produce intermediate δ values between the value typical of the pure molecular atmosphere ($\delta \approx 0.03$ with the CPL) and that value characteristic of the aerosol species.

The polarization lidar technique (Sassen, 2000, 2005a) has the unique ability to discriminate between spherical and nonspherical particles in the atmosphere, and thus determine unambiguously the thermodynamic phase of clouds. Furthermore, its sensitivity to particle shape can often facilitate identification of atmospheric aerosol type. Spherical aerosols (e.g., haze and aqueous smoke particles) produce little or no change in the polarization state of backscattered light, whereas nonspherical particles like dust can generate considerable depolarization depending on the exact particle shape and, to some extent, on the particle size relative to the incident wavelength (Mishchenko and Sassen, 1998). If the particle dimensions are smaller than the incident wavelength, reduced depolarization will be measured for a particular nonspherical particle due to the effects of the onset of Rayleigh scattering. For example, dust storm aerosols are relatively large and have a highly irregular shape, and typically generate δ of about 0.25 to 0.35, which is similar to many cirrus ice crystal clouds. Intermediate (and increasing) δ are found for aged (i.e., crystallized) sulfate haze and smoke aerosol, forest fire ash, tree pollen, and volcanic ash (Sassen, 2008). Fresh smoke aerosol sampled in Alaska (Sassen, 2008; Sassen and Khvorostyanov, 2008) typically generate near-zero δ (i.e., <0.03), but after transport aged smoke can produce values in the 0.05–0.10 range (Murayama et al., 2004). The phenomenon of increasing δ with particulate age occurs as the aerosol loses its moisture coating, exposing the irregular aerosol surface (Sassen et al., 1989).

ACPD
11, 16499–16552, 2011

2.2.2 Balloon-borne particle sampler

In-situ sampling of aerosols in the vertical profile over Fairbanks was conducted using a balloon-borne, step-integrating optical particle counter (an "OPC sonde"). A standard weather balloon conveys a sonde, built by Meisei Electric Company of Japan, that directly samples particulates ranging from 0.3 to 7.0 µm in diameter in eight size categories. It also returns temperature, humidity, and winds via GPS tracking. Particulate counts were quality-checked and used as recorded. This instrument has been successfully used in support of many other campaigns (e.g. Iwasaki et al., 2007; Hayashi et al., 1998). Data gathered by this instrument formed the basis of a detailed case-study conducted for 19 April 2008, the data for which will be treated separately in the results section.

2.2.3 Impact sampler

A three-stage DRUM impact sampler system is operated at the Poker Flat Launch facility 50 km north of the University of Alaska Fairbanks campus (e.g. Cahill, 2003). This instrument deposits aerosol material onto Mylar strips and provides relative counts in three size fractions for a range of chemical species. The DRUM sampler was operated continuously over the period 25 March through 30 April 2008 with a temporal resolution of 3 h. After field collection the aerosol samples are analyzed using Synchnotron X-Ray Flourescence (Cahill et al., 1999) for species identification. For this study a subset of species most broadly related to forest fire and haze (K and S) and mineral dust (Ca, Si and Fe) in a single size category (0.34–1.15 µm) were retained to help define the gross features of the temporal evolution of the period of study. A more thorough analysis of all the DRUM sampler species traces is provided in a companion paper.

ACPD
11, 16499–16552, 2011

2.2.4 Scanning Mobility Particle Spectrometer (SMPS)

Aerosols in the 12.6 to 280 nanometer diameter range were sampled at the Poker Flat Research Range with a TSI Scanning Mobility Particle Spectrometer (SMPS) system (Wang and Flagan, 1990). Observations were processed into 88 discrete size fractions and logged at five minute intervals. The SMPS, consisting of a TSI 3071 Differential Mobility Analyzer (DMA) and a TSI 3010 Condensation Nucleus Counter (CNC), operates in the following manner. The DMA initially establishes an aerosol ingest stream and prepares it for measurement by bringing the particulates to a state of charge equilibrium and then desiccating the stream. In parallel, a reference stream is generated from an ammonium sulfate solution. Finally, both streams are directed into the CNC where they are counted.

For this study, a principal components analysis was conducted on these data to reduce their dimensionality down to two main components. This allowed the time series to be defined in terms of the two broadest groupings of particulate sizes. A more detailed analysis of these data in conjunction with the sun photometer instrument (nephelometer), not discussed here, operated at the nearby Bonanza Creek Research facility, near UAF is being prepared for a companion paper.

3 Data collection and analysis

3.1 Overview of data time series

In general the results indicated four major atmospheric opacity events during the period 25 March–22 April. Temporal patterns of change were echoed in the results obtained from the lidar, drum sampler, and particle counter, which converged on four broad periods of aerosol activity:

1. Arctic Haze

ACPD
11, 16499–16552, 2011

2. Pristine
3. Dust plus smoke
4. Smoke

Below are presented for all instruments basic descriptions of their time series. A more integrated interpretation with trajectory plots in the context of weather patterns is provided later in the paper.

3.2 Polarization LIDAR

The lidar results indicated four broad periods that were distinguished from one another by the relative strength of the aerosol backscattering, depolarization, and/or depths and structures of the aerosol returns. From 1 April to around 7 April aerosol backscattering was extremely weak, confined to low altitudes, and very weakly depolarizing. Between 7 April and 13 April the aerosol concentration gradually built up but remained weakly depolarizing. On and after 14 April, however, the aerosol physical depth, backscattering strength, and depolarization all increased, and a layered aerosol structure began to appear as a typical feature. This progression is consistent with pristine Arctic conditions transforming to boundary layer Arctic haze, followed by the long-range transport of midlatitude aerosol at various levels in the atmosphere. Layering structures are often indicative of long-range travel. In these cases the more moderate depolarization levels indicate aged smoke aerosol or dust, or a combination of the two. Details of the lidar returns are provided below.

During the ARCTAS period at AFARS a total of 20, 1- to 2-h data acquisition sessions were conducted between 1 April and 1 May 2008. Observation timing was geared principally to coincide with afternoon overpasses of the A-train satellite formation and local ARCTAS-NASA aircraft flight activities. Data collection was not attempted during periods of low cloud and snowfall that would effectively block the lidar measurements.

The general evolution of the lidar signatures over the period of operation is discussed below (Fig. 2). In early April, lidar aerosol returns were typically quite weak in the

ACPD
11, 16499–16552, 2011

boundary layer (up to ∼2.0–3.0 km a.m.s.l.), and weakly depolarizing ($\delta \sim 0.02$–0.04), except at the lowest levels where depolarization was sometimes elevated up to ∼0.07. (These time averaged δ values are determined from time-averaged plots – not shown – using the summed returned signals in each channel at each height.) This can be interpreted as a mixture of diffuse Arctic haze and low-level urban pollution from the adjoining Fairbanks area. This low-level aerosol gradually built up until about 13 April. At this point two changes were noted: elevated aerosol layers made their initial appearance, and a shift to deeper, more strongly scattering aerosols occurred at both low and middle levels (in the absence of clouds). There is evidence for stronger lidar depolarization in some aerosol layers and in apparent aerosol veils associated with ice clouds (see below), but average δ remains relatively low, particularly near the surface. The peak 0.05–0.10 depolarization ratios are consistent with the transport of (aged) smoke particles, although concentrations of diffuse dust particles, or a combination of dust and smoke, is also possible. Clearly, however, the lidar data show an abrupt change in aerosol conditions and transport to this part of the Arctic that begins in mid-April.

The typical AFARS lidar height-time display examples given in Fig. 2 for the ARCTAS period illustrate these general findings. For each day identified at top, shown are pairs of δ value (see color scale at bottom) and relative returned (attenuated) lidar power displays in terms of a logarithmic gray scale (where white is the strongest range-corrected signal). These data were collected at the indicated times on 4, 9, 13, 15, 21, and 24 April and emphasize the transition from relatively pristine conditions to the onset of more pronounced and elevated aerosol content. They also show the character of the ice clouds, i.e., strongly depolarizing, that were frequently observed during this period that overlaid, or were associated with, the aerosols.

The example in Fig. 2a for the afternoon of 4 April is typical of the initial period showing only a weak boundary layer aerosol, beneath a ∼7.0–10.0 km high cirrus cloud layer generating $\delta \approx 0.5$. The top of the boundary layer at ∼3.0 km a.m.s.l. is sporadically marked by ice scud clouds composed of horizontally oriented plate crystals, which can generate near-zero depolarization, and only a weak decline in signal is evident aloft as

ACPD
11, 16499–16552, 2011

the laser pulse exits the diffuse haze layer. Although near the surface (all displays start at an altitude of 0.5 km a.m.s.l. because signals are unreliable in the first 200 m or so due to incomplete laser/receiver overlap) average $\delta \approx 0.07$ are present, they decrease to 0.02–0.03 higher in the boundary layer. This suggests a combination of low-level urban pollution from local power plants and other human sources, and weak Arctic haze in the boundary layer. By 9 April (Fig. 2b), the boundary layer haze is showing greater backscatter and some vertical structure.

The initial evidence for enhanced aerosol transport occurs late on 13 April (Fig. 2c). The mid-level altostratus cloud is dominated by ice and occasionally contains oriented ice plates, as well as a supercooled ($\sim -22\,^{\circ}$C) altocumulus cloud at ~4.5 km a.m.s.l. (note the bright, low-δ layer at around 21:00 UTC). In addition to the boundary layer Arctic haze ($\delta \approx 0.04$), a thin elevated aerosol layer is present at ~2.5 km a.m.s.l. with $\delta \approx 0.07$ before it disappears into the descending cloud base. This amount of depolarization indicates nonspherical particles, either too diffuse or small to generate higher δ, and corresponds to a dry air layer often associated with transported Asian dust or smoke layers. By early 15 April (Fig. 2d), the aerosol signal is considerably stronger and extends well into the mid-troposphere, at least well into the broken cirrus layer from 5.5–8.0 km MSL. The lidar aerosol returns are stratified into fine horizontal layers, a common observation associated with long-range transport. Lidar $\delta \approx 0.02$ are present near the surface, but increase to 0.07 in some of the aerosol layers (e.g., at 3.7 km), again suggesting a vertical gradient in spherical and nonspherical particles. The possible association of advected aerosols and cloud formation suggested by the data will be returned to below.

The displays for the afternoon of 21 April (Fig. 2e) reveal a shift to still more strongly backscattering and depolarizing aerosols. The aerosol is indicated to extend up to at least ~7.0 km a.m.s.l., and it is interesting to note the layer of enhanced backscattering at 4.5 km a.m.s.l. with $\delta \approx 0.09$ that seems related to aerosol processing in the evaporating cirrus cloud fallstreak noted prior to 21:00 UTC. Lidar depolarization in the near-surface aerosol layers ranges from 0.04–0.06. The final lidar displays for

ACPD
11, 16499–16552, 2011

24 April (Fig. 2f) again reveal a layered aerosol structure beneath cirrostratus cloud: the lower layer yields average $\delta = 0.05$, while the layer aloft at ~4.0 km a.m.s.l. generates δ of 0.15, the highest values noted during the ARCTAS period.

3.3 DRUM sampler: chemical species analysis

All of the aerosol concentrations obtained by this instrument at the Poker Flat Research Range during the ARCTAS experiment were low, with many element concentrations ranging below minimum detectable limits. The largest species concentration measured during the study was sulfur with a peak of 370 nanograms per cubic meter on 19 April (Fig. 3a). In addition, the largest concentrations of all of the aerosol components were present in the smaller size fractions (the 0.1 to 0.34 and 0.34 to 1.15 microns in aerodynamic diameter size fractions; not shown). This is consistent with larger particles settling out during transport and smaller particles growing into accumulation mode sizes through coagulation and gas-to-particle conversion during transport (Seinfeld and Pandis, 2006).

Four distinct, multiday "epochs" appear in the aerosol composition data as defined by variations in concentration. The periods are: (1) an "Arctic Haze" epoch during the last week of March, (2) a clean epoch during the first few days of April, (3) a smoke/dust epoch during the second week of April and (4) a smoke-dominated epoch during the third week of April.

The "Arctic Haze" epoch corresponds typically to trajectories that cross Northern Russia near Norilsk, a known Arctic Haze emission source area (Wilcox and Cahill, 2003). In this case, this Arctic Haze period possesses a mixed composition that includes a standard industrial tracer (Fig. 3b: Fe – Malm et al., 1994), slightly elevated wildfire species typical of a wildfire signature (Fig. 3a: S and K), and slightly elevated soil elements (Fig. 3b: Si, Ca).

The second epoch commences roughly 1 April and lasts to midday 5 April. This period has very low concentrations, on the order of a few nanograms per cubic meter, for all aerosol components.

ACPD
11, 16499–16552, 2011

The third epoch commences midday 5 April and lasts to roughly 17 April. All species commence a very rapid rise in concentration. Sulfur and potassium both spike quickly to 150 and 7 ng m^{-3}, respectively; after which both decline slowly over the next 12 days. Similarly, silicon, calcium and iron all spike quickly to 10, 8 and 3 ng m^{-3}, respectively; the spike exhibited by calcium is particularly strong. After approximately four days the values hold fairly consistently to the end of this epoch.

The fourth epoch commences roughly 17 April and runs to the end of record (28 April). After holding relatively steady through the third epoch the species trends now separate. Sulfur and potassium begin rising rapidly over the next four days, peak, and then descend again. Calcium begins a steady drop. Silicon and iron rise over the next four days then descend again, similar to sulfur and potassium but the relative extent of increase is lower.

3.4 Scanning Mobility Particle Spectrometer (SMPS)

The SMPS was operational during the following periods: 3 April–7 April, identified as the "early" period; and 15 April–22 April, identified as the "late" period. The principal components analysis was able to group the 88 individual size fractions into two prevalent patterns that together accounted for 90 % of the variance. Scoring patterns for the first component showed generally elevated concentrations in the early period that possess some variability and drop off in the late period (Fig. 4); that is, this is representing those size fractions which exhibited elevated concentrations in the early period and low concentrations in the late period. Sporadic, abrupt spikes correspond to many of the concentration peaks observed in the raw data traces (not shown) and indicate, for the early period, moderate concentrations at the beginning with rapid spikes to a high concentrations partway through, and a rapid drop to very low levels by the end. Loading patterns (not shown) indicate smaller size fractions (126 nm–≈1000 nm) tended to be loaded against this pattern and that the general trend of the pattern went from positive in the in early period to negative in the late period following a rapid transition midway through, with a negative loading representing correspondence to the inverse sense of

ACPD
11, 16499–16552, 2011

the scoring time series. In general, the first component is indicating the broadest scale features in the temporal evolution of the concentration patterns. Scoring patterns for the second component (Fig. 4) were opposite those for component one, reflecting size fractions that had low concentrations in the early period and higher concentrations in the later period. Loading patterns (not shown) indicate this pattern was more reflective of larger size fractions (≈1000 nm–2890 nm). The raw traces (not shown) indicated, at ∼14 h, 5 April, the onset of a rapid rise in concentration values for size fractions represented by this component. Late period values were higher than the early period values.

3.5 Regional-scale climate

3.5.1 Mean patterns

The bulk of the Alaska region is situated far enough to the north to place it north of the polar jet stream in winter, and well in its path in the summer. April is a transition season – regionally, patterns typical of winter still dominate, which can include large portions of the Interior coming under the influence of a surface-based density high, upper levels dominated by a corresponding weak low, and large-scale flow patterns dominated by a jet stream flow moving along or south of the Aleutian Islands. Periods of strong southerly flow into Interior Alaska, which occur during marked departures from zonal flow, are becoming more frequent in April than in winter as the jet stream moves north.

By mid-April the day length in interior Alaska is exceeding 15 hours with a maximum solar elevation approaching 40°. Roughly half of the days in April can expect clouds. Typically snow is still on the ground at least through mid month. This results in the local scale near the ground remaining dominated by snow- and ice-covered surfaces which inhibit radiation-based heating and favor surface inversions, despite the rapidly increasing influx of shortwave radiation. Typically, the inversion pattern transitions from a semi-permanent inversion situation in January/February, associated with

ACPD
11, 16499–16552, 2011

the low radiation input and broken only by strong synoptic forcing, to one in which the inversion settles in overnight and is broken during the day.

3.5.2 Climate patterns during ARCTAS/ARCTEX, 5–19 April 2008

The most prominent climatological feature exhibited during the timeframe of the ARCTAS experiment was a strong high pressure anomaly in the Gulf of Alaska/south Bering Sea, noted by Fuelberg et al. (2010) in their discussion. This pattern favored the direction of flow into the Gulf of Alaska and the western, northern and Interior parts of Alaska in April 2008 (Fig. 5), which is not the typical pattern for April (Fig. 6). During some periods at some levels, the pressure pattern to the west of the Bering Sea was arranged such that air masses originating from the mid- and northern-Siberian regions were directed towards the Bering Sea area, and from there on into the Alaska region. The climatological mean pattern for this period does exhibit flow moving across the same region of Siberia, but the air mass is directed southeasterly, out into the North Pacific where, after a relatively lengthy trip, it can reach Interior Alaska from the southeast, around one of the transient low pressure systems that are frequently found in the Gulf of Alaska at this time.

During the first part of April, up to ~16 April, a general pattern of weak northwesterly flow was in place over the Interior. This was characterized near the surface by low moisture content and little cloud cover, with correspondingly cool temperatures in the −10 to −20 °C range. This allowed for a strong diurnal variation in surface air temperature with a nighttime radiation inversion of several hundred meters depth. During this time the dominant pressure pattern control was a strong area of high pressure situated over the Aleutian Islands (Fig. 6). By the second week in April a low pressure system had approached from the southwest, moving up the east side of Kamchatka Peninsula, and displaced the high towards the east and established a west/southwesterly flow over the Interior. This initiated a pattern whereby Interior Alaska was dominated by a pronounced strong, anomalous, westerly/southwesterly flow throughout the lower- to middle-levels of the atmospheric column (925 mb, 700 mb, 500 mb). This brought

ACPD
11, 16499–16552, 2011

unusually cool temperatures at the lower levels (coolest near surface, warming to neutral anomaly at ~3000 m) and unusually warm temperatures at higher levels (warm anomaly increasing above ~4000 m). It also caused an increase in air mass moisture content and temperatures. Cloud cover increased and surface diurnal cycling ceased. By 18 April the anomalous high pressure zone had shifted southeastwards, moving from the south Bering Sea to lie in the central Gulf of Alaska, with associated flow coming from the north Pacific. In response, temperatures at the low levels warmed to become positive anomalies.

4 The 19 April case study: balloonsonde results

The OPC balloonsonde was launched at Fairbanks at 22:00 UT 19 April and gathered aerosol size distribution data continuously from 198 m up to 8500 m (Fig. 7), after which the balloon disintegrated and the OPC unit returned to earth for recovery. Size distributions ranged from 0.3 to 7.0 µm in diameter. Size criteria were calibrated against a refractive index of 1.4-0i. Background atmospheric conditions consisted of, at the surface, calm winds with a moderate humidity of ~40 %. Up into the vertical profile wind speed slowly increased with height, to ~15 m s^{-1} by 4000 m, and settled on a consistent west-northwesterly direction. Between 1 and 2.2 km the atmosphere was very dry (Fig. 7). The lower levels of the atmosphere were very stable, as inferred from radiosonde data (not shown), and similar conditions existed in the days leading up to 19 April. This suggests that minimal contribution is to be expected from Fairbanks urban sources to the aerosol load observed above the strong diurnal inversion layer because the launch took place away from town.

In support of the OPC sonde launch the AFARS lidar was operated from 18:00 UT to 23:50 UT on 19 April (Fig. 8). General results from this instrument indicate distinct horizontal banding up to ~5.0 km a.m.s.l. due to stratified aerosol layers which display δ ranging from 0.05–0.09. Before 20:30 UT and above ~5.0 km are found sporadic, thin cloud layers which top out at 8–12 km with cirrus. The height of the cirrus cloud

ACPD
11, 16499–16552, 2011

top, i.e. 12.0 km a.m.s.l., is indicative of an elevated tropopause. After 21:00 UT this cloud can be seen to rapidly transition to a deep altostratus cloud that is optically dense enough to attenuate the laser pulses. Coincident data taken at the AFARS facility by the W-band radar Doppler radar (not shown) measured downward velocities of 2.0 m s^{-1} in the midlevel fallstreaks, indicative of large ice crystal aggregates. The combined results from both instruments is discussed in more detail in Sect. 4.1.

Vertical profiles of size distributions for the eight aerosol size fractions returned by the OPC indicated the presence of discernible layers (Fig. 9). In general, total aerosol loading in the lowest 4.1 km was very high, approaching 100 particles cm^{-3} even in the free troposphere up to 3.5 km, with a reduction to ~50 particles cm^{-3} above 3.5 km (Fig. 10). When broken down by size fraction, counts exhibited strong differences. Counts for the two largest size fractions are very low, decreasing up the profile from a maximum at the surface. Counts for the mid-range sizes – ~1 µm – were relatively low, and counts for the finer size fractions and the 2 and 5 µm size fraction range were higher (Fig. 10), with counts in the smallest size fractions (60–240 nm) highest at least for the level of measurement, around ~500 m a.m.s.l. (Fig. 11).

The most readily noticeable layer feature is the transition that occurs above 4.1 km. In this layer the largest size fractions exhibit a rapid increase in concentration, indicating that the OPC penetrated an ice cloud. In this case, the OPC is counting ice crystals as large aerosols, which explains the rise in the larger fractions while the smaller size fractions are relatively unchanged. Additional cloud layers are evident in the profile up to 8.5 km; i.e., the deep altostratus layer described previously. An interesting feature to note is the strong drop in small size fractions in the layers between the clouds, possibly indicative of scavenging. The region of interest in the profile for this case study, however, is the cloud-free lowest 4.1 km.

OPC/lidar results integration

By integrating the results from the OPC and the AFARS lidar six distinct layers may be identified in the lowest 4.1 km, summarized in Table 1 and displayed in Fig. 8. For

ACPD
11, 16499–16552, 2011

greater clarity of vertical trends the OPC data are also presented as absolute counts by size fraction and by layer (Fig. 10), and as absolute volumes of particulate per unit volume of air, again by size fraction and by layer (Fig. 11). The first, lowest layer, extending from the surface to ~330 m, is the only layer with relatively high concentrations of particulates in the largest size fractions. This is a result of urban combustion activities trapped in the surface-based inversion that tends to set up in Fairbanks in the absence of strong synoptic forcing. Examination of the radiosonde launch from 12:00 UT 19 April (10 h earlier – not shown) confirmed the presence of a strong primary inversion from the surface to ~300 m, a thin non-inversion layer of ~100 m in thickness, and a weaker, secondary inversion up to ~1100 m. Because the particulate loadings for this layer are so heavily influenced by local factors it is identified as "layer 0" and is not considered further in the same manner as the layers of atmosphere above it, which are less influenced by the surface.

A second layer (identified as layer 1) extending from 330 m–1080 m may be discerned from various sources: OPC, lidar, and humidity data. The OPC showed elevated counts in the mid-sized fractions (0.5 through 3.0 µm), lidar returned higher backscatter ratios (approaching 0.1), and humidity decreased. The two largest size fractions are most strongly represented in this layer because it becomes part of the stable boundary layer during the night, entraining these size fractions (local combustion products), which then do not have enough time to settle out during the day.

A third layer (identified as layer 2) extended from 1080 m–2230 m. This layer is most strongly identified in the humidity trace and the lidar profile. It is the driest part of the profile – relative humidity is ~20 % throughout the layer. The largest size fractions on the OPC traces are relatively high throughout the layer, with low concentrations at the top and bottom, although volumetric concentrations of small size fractions were almost double that of the large fractions. The lidar indicates this layer possesses the lowest depolarization ratios in the profile.

The next layer (identified as layer 3) extended from ~2400 m–3020 m. This layer was characterized by strongly increasing humidity and a profile maxima for 2–5 µm

ACPD
11, 16499–16552, 2011

size fractions in the OPC (Fig. 11), which exceeded that of the smaller size fractions by 50 %. This layer exhibited much higher depolarization ratios in the lidar profile.

Layer 4, extending from 3020 m–3450 m, exhibited moderate concentrations in the smallest and the ~3 µm size fractions. It also possessed the highest humidity below the cloud layer. Lidar depolarization remained high in this layer although at the bottom part of the layer depolarization was a little lower. Although overall volumetric counts were lower than observed in layer 3, the ratio of large particles to small remained high, similar to layer 3.

The final layer, layer 5, extended from 3450 m–~4100 m; up to the cloud base. All OPC size fractions dropped off in this layer, with the smallest size fractions exhibiting the sharpest decline. The ratio of large particles to small was again high in this layer. Humidity is relatively low until the cloud base, and lidar depolarization remained high. Note that, for all layers except layer 5, the size fraction ~1–1.5 µm possessed the lowest concentrations. Peaks at the smaller and larger fractions are indicative of aerosols small enough to be transported long distances without settling out and large aerosols most likely derived from Asian dust particles in combination with Asian smoke particles.

5 Discussion

The establishment of four, distinct aerosol loading epochs over the timeframe 25 March–30 April is supported by all three time series data sets. The Impact Drum sampler traces are the most continuous over the period and lay the foundation for clear identification of aerosol epoch timing. The lidar profiles available during most days of the experiment exhibited backscatter distribution patterns and strengths and depolarization ratios that indicated several aerosol events during this time containing mineral dust, smoke, or most likely, a mixture of the two. Lidar measurements are in turn supported by the OPC-sonde data profiles which matched the larger particulates in dry layers with high lidar backscatter ratios. The SMPS data, while missing a large section in the middle of April, still indicate the transition from the second (pristine) to the

ACPD
11, 16499–16552, 2011

third (smoke + dust) epoch, and further support a fourth epoch (smoke) as distinct from the third. Climatologically, indications of the general nature of departure of this period from climatology have been highlighted here, as treated in greater depth in Fuelberg et al. (2010). With that groundwork established, this section will lay out the synoptic progression in greater detail for each aerosol epoch identified in the results. This will include an integrated discussion of the epochs in terms of synoptic patterns, as supported by trajectory analyses.

5.1 Arctic Haze epoch

The synoptic pattern during the Arctic Haze epoch was dominated by a strong low pressure region situated over the East Siberian Sea with a trough extending to the east linking up with a secondary center of low pressure situated over the Bering Sea. This resulted in a flow pattern that passed over Northern Russia near Norilsk, a known Arctic Haze emission source area (Wilcox and Cahill, 2003), moved east across northern Siberia, entrained around the Bering Sea low feature and finally advected over the Alaska Interior (Fig. 12). This pattern in general is not unusual for this time of year, however there were departures from climatology which took the form of a stronger and more compact low pressure feature over the East Siberian Sea. This pattern shifted the flow path farther to the north/northeast than would typically be observed for this period. This likely served to isolate the northern airmass, reducing contamination by smoke or dust from source regions situated farther south and resulting in a "classic" haze signature as observed by both the lidar and the drum sampler, the two instruments taking observations during this time. The relatively long distance travelled by the air mass from its source provided ample opportunity for pollutant concentrations to mix out, which is likely responsible for the relatively low signature strength observed by both ground instruments. Note that during this period the flow into the Alaska Interior was enhanced, both in terms of gradient (speed) and directionality, by the presence of

ACPD
11, 16499–16552, 2011

a high pressure region in the northeastern Gulf of Alaska, which was another departure from climatology.

5.2 Pristine epoch

Starting 1 April and over the next few days the strong low pressure center situated over the East Siberian Sea weakened and became more symmetric, losing the eastern trough feature. At the same time a second strong low pressure center developed east of Japan and moved slowly to the north-northeast. By 2/3 April these two features joined to form a broad zone of low pressure extending from the Kara Sea to the Bering Sea. The Bering Sea dipole possessed a deep trough extending well to the southwest. While the low pressure merger was happening, a strong and climatologically anomalous high pressure region developed in the central North Pacific. The net result of this pattern was the direction of flow into the Alaska Interior from the western North Pacific Ocean by way of the Alaska Range (Fig. 13). This combination meant that entrained air parcels (a) started in a relatively clean region, (b) had little potential to entrain aerosols due to lack of contact with terrestrial source regions, (c) spent an extended period over the northwest Pacific Ocean, providing opportunity for aerosol loss due to settle-out and due to scavenging by wet deposition processes (e.g. Sect. 3.3), and (d) experienced forced orographic ascent, again allowing opportunity for wet deposition/precipitation loss. The combination of these factors and processes likely contributed to greatly reduce the aerosol loading, resulting in the extraordinarily clear conditions recorded by the lidar and drum sampler from 1 April to midday 5 April that immediately preceded the initiation of ARCTAS activity. One interesting exception was the SMPS sensor: the larger size fractions matched the pattern indicated above, but the smallest size fractions did not. During the pristine period, while not strongly elevated, they did exhibit fluctuations. This was identified in the principal components analysis (Fig. 4). This is presumed to be a local-source contribution from the urban boundary layer when winds favored plume advection over the SMPS site to the east of town (Bonanza Creek). An

ACPD
11, 16499–16552, 2011

examination of Fairbanks regional winds (not shown) indicated a period of elevated low level winds at this time.

5.3 Smoke/dust epoch

Around midday on 5 April all Interior sensors recorded a very rapid onset of aerosol loading at the surface and at various layers in the vertical column. At this time the loading was characterized by the lidar and the drum sampler as likely dominated by crustal aerosol species; before it ceased recording on 6 April the SMPS recorded the onset of larger size fraction loading, further indication of a major change in loading type. In particular the drum sampler traces showed a clear crustal signature with calcium, silicon, and other soil elements being elevated as well as a strong wildfire smoke signature, characterized by large potassium concentrations (Malm et al., 1994; Cahill et al., 2008). Sulfur is also elevated during this period, which is consistent with wildfire emission.

Establishment of a large-scale flow pattern able to advect aerosols over the Alaska Interior was initiated by a weakening of the trough feature off the Bering Sea low, replaced by the establishment of a more zonal pattern in the north, anchored in the west by the persistent Siberian coast (Kara Sea) low, and in the east by the now smaller, but persisting, low over the northern Bering Sea. Note that the Kara Sea low exhibited a strong southern trough extension at this time. Finally, a low pressure system formed over Japan and moved slowly north northeastward towards Kamchatka, establishing a broad area of low pressure along the Asian east coast up to the Bering Sea. Combined, these features set up a flow trajectory directed initially to the southeast over the Lake Baikal/Mongolian region, east-northeastward towards the Aleutians, then along the south side of the Japan/Bering Sea low and over the Alaska interior without transiting the Alaska Range (Fig. 14). This flow pattern represents a fairly direct pathway from north China/southern east Siberia, which was maintained over the next few days by the continued presence of the high pressure feature in the central North Pacific. Thus, in contrast to the pristine period, air masses advected over the Interior

ACPD
11, 16499–16552, 2011

after 5 April were spending less time over the ocean and were not traversing the Alaska Range. These pathways are suggested by a pressure analysis and supported by back-trajectories (Figs. 15 and 16). During this period fires were burning in the Kazakhastan region (agricultural) and southern Siberia, near the northern Mongolia border (boreal forest). Warneke et al. (2009) indicate the unusually early start to the fire season this represented. In late March and very early April boreal fire emissions were not well established; the predominant source was the agricultural burning component. The pathway indicated in Fig. 16 would entrain smoke from this region and bring it over Alaska.

The occurrence of crustal species, unlike smoke, requires a suitable synoptic event at the point of origin to get the aerosols into the air. Synoptic analysis suggested two possible dust-loading events that could have introduced these species for possible transport. The first commenced 28 March over central Asia, where a compact high pressure feature developed over eastern Kazakhstan. This established a strong pressure gradient with flow directed south across eastern Kazakhstan in the region of the Takla Makan Desert; flow then turned eastward across the northern region of China, in the vicinity of the Gobi Desert (Fig. 17). Wind speed estimates from NCEP/NCAR reanalysis exceeded 20 m s^{-1}, more than sufficient to raise dust into the atmosphere (Australian Bureau of Meteorology). The K-lifting index was also elevated over the Takla Makan Desert region, suggesting instability sufficient to move raised dust into the atmosphere for transport. The second event commenced 2 April. A strong pressure gradient was established across the Gobi Desert. The strong winds accompanying this event were associated with a cold front leading a cold air outbreak that pushed southeastwards through eastern Mongolia and into northern China (Fig. 18). Various authors point out that raised dust events occur every year in the Gobi and Takla Makan region during the March–May season (Lee et al., 2006; Wetzel et al., 2003; Cahill, 2003); the observation of crustal species in the aerosols reaching the Alaska Interior given favorable large-scale flow patterns is therefore not an unexpected occurrence.

ACPD
11, 16499–16552, 2011

5.4 Smoke epoch

The final period was defined by another major change in drum sampler species traces that occurred 17–18 April. Ground-based observations, specifically the assessment of chemical species, suggested that at this time the aerosol loading transitioned to become more dominated by smoke with a relative reduction in crustal signature. Potassium and sulfur concentrations exhibited a large increase; the crustal element concentrations (except Fe) increased to 19 April then decreased after that (Fig. 3b).

The large-scale synoptic pattern was dominated by a broad region of low pressure that was established north of Mongolia and a stronger low pressure zone over Kamchatka (Fig. 19). The high pressure over the North Pacific persisted. This established a flow pattern that could advect parcels directly over known fire zones in eastern Kazakastan and just south and east of Lake Baikal, and away from the desert regions farther south. Boreal forest fires by this time in April were well underway in southern Siberia (Fig. 20).

The OPC-sonde case-study ascent was conducted on 19 April. The detailed profile loading data provided a means to verify and understand in greater detail what the lidar was seeing. Three main features emerged. First is the presence of the elevated large size fraction loading in the lowest levels. For level 0 this was clearly associated with combustion by-products from the Fairbanks area, trapped in the continuous surface-based inversion layer that dominated this time period. The elevated large particle count for layer 1, however, reflected the higher level diurnal component of the inversion that sets up at night. Combustion particles are entrained in this layer when fully developed during the night such that, even though it decouples from the surface inversion later in the day, it still retains high loading of large particulates. The second main feature is the presence of elevated large particulate loading aloft. These are not as large as the combustion particles and are not locally derived but likely represent Asian dust that has been advected in, as suggested by the back trajectory plots. The depolarization ratios in these layers are relatively high, indicative of large particles that do not possess a

ACPD
11, 16499–16552, 2011

surface water layer, which means either hydrophobic mineral particles from desert dust or humid smoke particles dessicated by long-range transport. Although smoke particles can give depolarization ratios as high as 8 % after high rates of drying experienced during lengthy transport, the depolarization ratio is high enough – approaching 9 % – to suggest at least an inclusion of desert dust. This is also supported by the drum sampler data, which exhibited peak in crustal species concentration on 19/20 April. The back trajectory does support this idea because traces over the Takla Makan/Gobi Desert regions are indicated. The third main feature is the fact that the atmospheric constituents are arranged in discrete layers. This is also indicative of long-range transport.

Finally, the Scanning Mobility Particle Spectrometer (SMPS) north of Fairbanks was being operated in the days around 19 April. Most prominently, this instrument indicated an elevated loading of small aerosols (120–250 nm) during the period of the OPC sonde launch (Fig. 21).

6 Summary

In general, it should be pointed out that in comparison to earlier spring-transition months (March through May) from AFARS, the ARCTAS period data seems unusual in that more dramatic and highly depolarizing aerosol episodes are lacking. This is particularly apparent because of the absence of strongly scattering aerosol layers derived from Asian dust storms (Sassen, 2005b). Forest fire smoke episodes transported from northern China and eastern Russia are also not uncommon at AFARS in spring. It is suggested that aerosols of mixed composition (haze, dust and aged smoke) and relatively small size and concentration were dominant, perhaps affected by cloud processing between the midlatitude source region and AFARS. It is also intriguing that, after the indicated onset of midlatitude mixing in mid-April, at midlevels the cirrus and other ice clouds often appear to be associated with diffuse aerosol layers. It has previously been shown from AFARS that springtime ice cloud formation can be linked to

ACPD
11, 16499–16552, 2011

the presence of midlatitude aerosols transported to the previously clean Arctic region (Sassen, 2005b).

Given that the elemental compositions observed by the drum sampler are consistent with known source emissions from the areas crossed by the trajectories, it appears that at least some of the upper level aerosols are being mixed downwards in the atmosphere. However, the low concentrations at ground level and the higher altitude aerosol layers observed by the lidar imply that only a small fraction of the upper-level aerosol plumes have been mixed downwards. This is consistent with the strong zone of stability in the lowest levels of the boundary layer in the Alaska Interior; on many occasions it is decoupled from the higher level atmosphere and mitigates vertical mixing.

An important aspect of this paper has been the case made for the existence of a robust mineral component in the aerosol loadings. A lot of attention has been focused on the agricultural and boreal forest fire sources by other papers resulting from the ARCTAS and corresponding NOAA ARCPAC efforts, which was a primary scientific objective for ARCTAS. However, Interior Alaska ground-based instrumental results, combined with trajectory traces and detailed central Asian synoptic assessments, do argue for the inclusion of a mineral source load in the plumes advected over this region during the second week of April 2008. The inclusion of mineral sources in aerosol loading is of potential importance, especially in the north. In their review, Haywood and Boucher (2000) overviewed the radiative effects of mineral aerosols as published in various sources. The general conclusion, while variable, indicated a negative effect due to reduction of solar radiation and a slightly larger positive effect due to absorbed upwelling thermal radiation. This net positive forcing was noted to be larger in areas of high surface albedo.

The sensitivity of Alaska atmospheric loading is apparent in the speed and extent to which the aerosol load can change as the synoptic situation evolves. The observations conducted during the time-frame of ARCTAS-A provided examples of four major loading types over Alaska: “classic” arctic haze, as defined by industrial emissions transported by a high-latitude zonal pattern; less-common pristine clear skies resulting from

ACPD
11, 16499–16552, 2011

low pressure feature situated to the west of Alaska; dust, caused by a lifting event over Asia and favorable trajectory that included an anomalous north Pacific high that shifted the trajectory farther north; and smoke, caused by a strong and early start to the Asian boreal fire season and the anomalous dust trajectory noted above. The strong loading period wound down towards the end of April as the north Pacific high was slowly replaced by the more typical expansive low-pressure system, with the trajectory directed along progressively lengthier pathways before reaching the Alaska Interior (Fig. 22). Lidar and balloonsonde observations laid the groundwork for establishing likely aerosol type as dust and aged smoke; strongly layered structures also indicated lengthy transport. Surface based drum sampler and SMPS provided details about aerosol type, again indicating their terrestrial and fire origins. Despite the activity noted during the observing campaign, the strength of the synoptic pattern anomaly suggests that the aerosol patterns observed in April of 2008 are in general not to be expected over the Alaska Interior at this time of year.

Acknowledgements. The authors wish to express their gratitude to the following agencies and projects that made this work possible: National Aeronautics and Space Agency (NASA) grant 07-ARCTAS08-0050, National Science Foundation (NSF) grants ATM-0630506 and AGS-1037000 for the AFARS research facility (K. Sassen), and National Oceanic and Atmospheric Administration (NOAA) grant NA06OAR460017 (D. Atkinson). We also wish to express our thanks to formal and discussion reviewers who contributed their time to improving this paper.

References

Australian Bureau of Meteorology, Web page referenced: http://reg.bom.gov.au/nsw/sevwx/facts/dust.shtml, last access: 18 February, 2011.

Cahill, C. F.: Asian aerosol transport to Alaska during ACE-Asia, J. Geophys. Res., 108(D23), 8664, doi:10.1029/2002JD003271, 2003.

ACPD

11, 16499–16552, 2011

Cahill, T. A., Cliff, S. S., Perry, K. D., Jimenez-Cruz, M. P., and McHugo, S. A.: Size and time resolved anthropogenic components of aerosols via synchrotron X-ray fluorescence: Application to Asian aerosol transport, EOS Transactions of the American Geophysical Union, 80(46), Fall Meeting Supplement, Abstract A12C-09, 1999.

Cahill, C. F., Cahill, T. A., and Perry, K. D.: The Size- and Time-Resolved Composition of Aerosols from a Sub-Boreal Forest Prescribed Burn, Atmos. Environ., 42, 7553–7559, doi:10.1016/j.atmosenv.2008.04.034, 2008.

Fuelberg, H. E., Harrigan, D. L., and Sessions, W.: A meteorological overview of the ARCTAS 2008 mission, Atmos. Chem. Phys., 10, 817–842, doi:10.5194/acp-10-817-2010, 2010.

Hayashi, M., Iwasaka, Y., Watanabe, M., Shibata, T., Fujiwara, M., Adachi, H., Sakai, T., Nagatani, M., Gernandt, H., Neuber, R., and Tsuchiya, M.: Size and Number Concentration of Liquid PSCs: Balloon-Borne Measurements at Ny-Alesund, Norway in Winter of 1994/95, J. Meteorol. Soc. Jpn., 76, 549–560, 1998.

Haywood, J. and Boucher, O.: Estimates of the Direct and Indirect Radiative Forcing due to Tropospheric Aerosols: A Review, Rev. Geophys., 38, 513–543, 2000.

Iwasaki, S., Maruyama, K., Hayashi, M., Ogino, S.-Y., Ishimoto, H., Tachibana, Y., Shimizu, A., Matsui, I., Sugimoto, N., Yamashita, K., Saga, K., Iwamoto, K., Kamiakito, Y., Chabangborn, A., Thana, B., Hashizume, M., Koike, T., and Oki, T.: Characteristics of aerosol and cloud particle size distributions in the tropical tropopause layer measured with optical particle counter and lidar, Atmos. Chem. Phys., 7, 3507–3518, doi:10.5194/acp-7-3507-2007, 2007.

Jacob, D. J., Crawford, J. H., Maring, H., Clarke, A. D., Dibb, J. E., Emmons, L. K., Ferrare, R. A., Hostetler, C. A., Russell, P. B., Singh, H. B., Thompson, A. M., Shaw, G. E., McCauley, E., Pederson, J. R., and Fisher, J. A.: The Arctic Research of the Composition of the Troposphere from Aircraft and Satellites (ARCTAS) mission: design, execution, and first results, Atmos. Chem. Phys., 10, 5191–5212, doi:10.5194/acp-10-5191-2010, 2010.

Kalnay, E., Kanamitsu, M., Kistler, R., Collins, W., Deaven, D., Gandin, L., Iredell, M., Saha, S., White, G., Woollen, J., Zhu, Y., Leetmaa, A., Reynolds, R., Chelliah, M., Ebisuzaki, W., Higgins, W., Janowiak, J., Mo, K. C., Ropelewski, C., Wang, J., Jenne, R., and Joseph, D.: The 1996 NCEP/NCAR 40-Year Reanalysis Project, B. Am. Meteorol. Soc., 437–471, 1996.

Lee, H. N., Igarashi, Y., Chiba, M., Aoyama, M., Hirose, K., and Tanaka, T.: Global Model Simulations of the Transport of Asian and Sahara Dust: Total Deposition of Dust Mass in Japan, Water Air Soil Poll., 169–137, 2006.

ACPD
11, 16499–16552, 2011

Malm, W. C., Sisler, J. F., Huffman, D., Eldred, R. A., and Cahill, T. A.: Spatial seasonal trends in particle concentration and optical extinction in the United States, J. Geophys. Res., 99, 22357–22368, 1994.
Mishchenko, M. I. and Sassen, K.: Depolarization of lidar returns by small ice crystals: An application to contrails, Geophys. Res. Lett., 25, 309–312, 1998.
Murayama, T., Müller, D., Wada, K., Shimizu, A., Sekiguchi, M., and Tsukamoto, T.: Characterization of Asian dust and Siberian smoke with multi-wavelength Raman lidar over Tokyo, Japan in spring 2003, Geophys. Res. Lett., 31, L23103, doi:10.1029/2004GL021105, 2004.
Sassen, K.: Lidar Backscatter Depolarization Technique for Cloud and Aerosol Research, in: Light Scattering by Nonspherical Particles: Theory, Measurements, and Geophysical Applications, edited by: Mishchenko, M. L., Hovenier, J. W., and Travis, L. D., ISBN 0-12-498660-9, Academic Press, 393–416, 2000.
Sassen, K.: Polarization in Lidar, in: Lidar, edited by: Weitkamp, C., Springer Press, Berlin, 19–42, 2005a.
Sassen, K.: Dusty ice clouds over Alaska, Nature, 434, 456, 2005b.
Sassen, K.: Identifying Atmospheric Aerosols with Polarization Lidar, in: Advanced Environmental Monitoring, edited by: Kim, Y. J. and Platt, U., Springer-Verlag, Berlin, 136–142, 2008.
Sassen, K. and Khvorostyanov, V. I.: Cloud effects from boreal forest fire smoke: Evidence for ice nucleation from polarization lidar data and cloud model simulations, Environ. Res. Lett., 3, 025006, doi:10.1088/1748-9326/3/2/025006, 2008.
Sassen, K., Zhao, H., and Yu, B.-K.: Backscatter laser depolarization studies of simulated stratospheric aerosols: Crystallized sulfuric acid droplets, Appl. Optics, 28, 3024–3029, 1989.
Seinfeld, J. H. and Pandis, S. N.: Atmospheric Chemistry and Physics – From Air Pollution to Climate Change, 2nd edition, John Wiley & Sons, 2006.
Shaw, G. E.: The Arctic Haze Phenomenon, B. Am. Meteorol. Soc., 76(12), 2403–2413, 1995.
Wang, S. H. and Flagan, R. C.: Scanning Electrical Mobility Spectrometer, Aerosol Sci. Tech., 13, 230–240, 1990.
Warneke, C., Bahreini, R., Brioude, J., Brock, C. A., de Gouw, J. A., Fahey, D. W., Froyd, K. D., Holloway, J. S., Middlebrook, A., Miller, L., Montzka, S., Murphy, D. M., Peischl, J., Ryerson, T. B., Schwarz, J. P., Spackman, J. R., and Veres, P.: Biomass burning in Siberia and Kazakhstan as an important source for haze over the Alaskan Arctic in April 2008, Geophys. Res.

ACPD
11, 16499–16552, 2011

Lett., 36, L02813, doi:10.1029/2008GL036194, 2009.
Wetzel, M. A., Shaw, G. E., Slusser, J. R., Borys, R. A., and Cahill, C. F.: Physical, Chemical and Ultraviolet Radiative Characteristics of Aerosol in Central Alaska, J. Geophys. Res., 108(D14), 4418, doi:10.1029/2002JD003208, 2003.
Wiedensohler, A.: An approximation of the bipolar charge distribution for particles in the submicron range, J. Aerosol Sci., 19, 387–389.1988.
Wilcox II, W. J. and Cahill, C. F.: Regional Haze Trends in Alaska: Implications for Protected Class I Visibility Areas, EM, Dec. 2003, 34–39, 2003.

ACPD
11, 16499–16552, 2011

Table 1. Layers present in the lowest 4.1 km of the atmosphere for the Fairbanks area, 22:00 UTC, 19 April 2008, as derived from OPC observations.

Layer	Height range	Defining features	Apparent cause
0	188–330 m	Maxima in largest size fractions	Urban combustion byproducts trapped by the very strong surface-based inversion
1	330–1080 m	Rise in mid-range size fractions, RH drop, elevated depolarization ratio	Haze layer trapped under weaker secondary inversion
2	1080–2230 m	Low and steady RH, low depolarization ratio	Relatively large numbers of small particles
3	2400–3020 m	Rapidly rising RH, maximum depolarization ratio in entire column	Dust
4	3020–3450 m	RH maximum, high depolarization ratio	
5	3450–4100 m	RH decrease before cloud, high depolarization ratio	Cloud scavenging of small aerosols, larger sea-salt particles

ACPD
11, 16499–16552, 2011

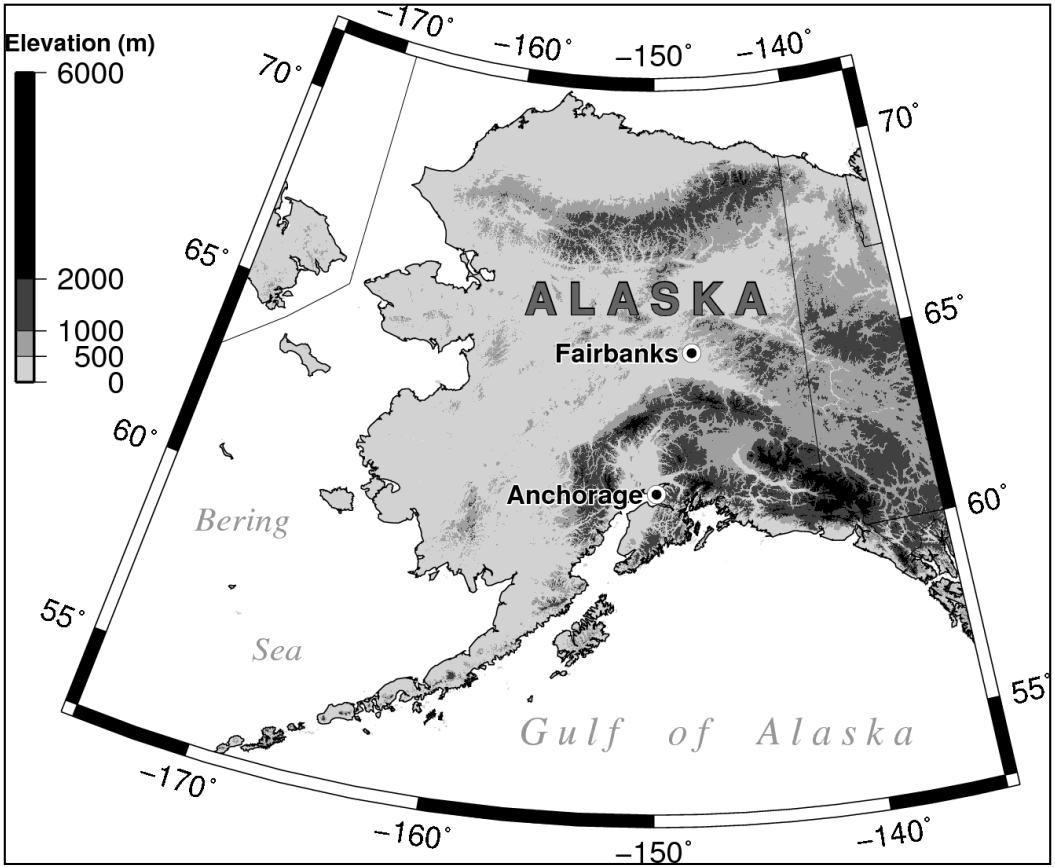

Fig. 1. Alaska showing the topographic context of Fairbanks and the Alaska Interior. Surface data were obtained at locations in Fairbanks or at the Poker Flat Launch Facility, 50 km north of Fairbanks.

ACPD
11, 16499–16552, 2011

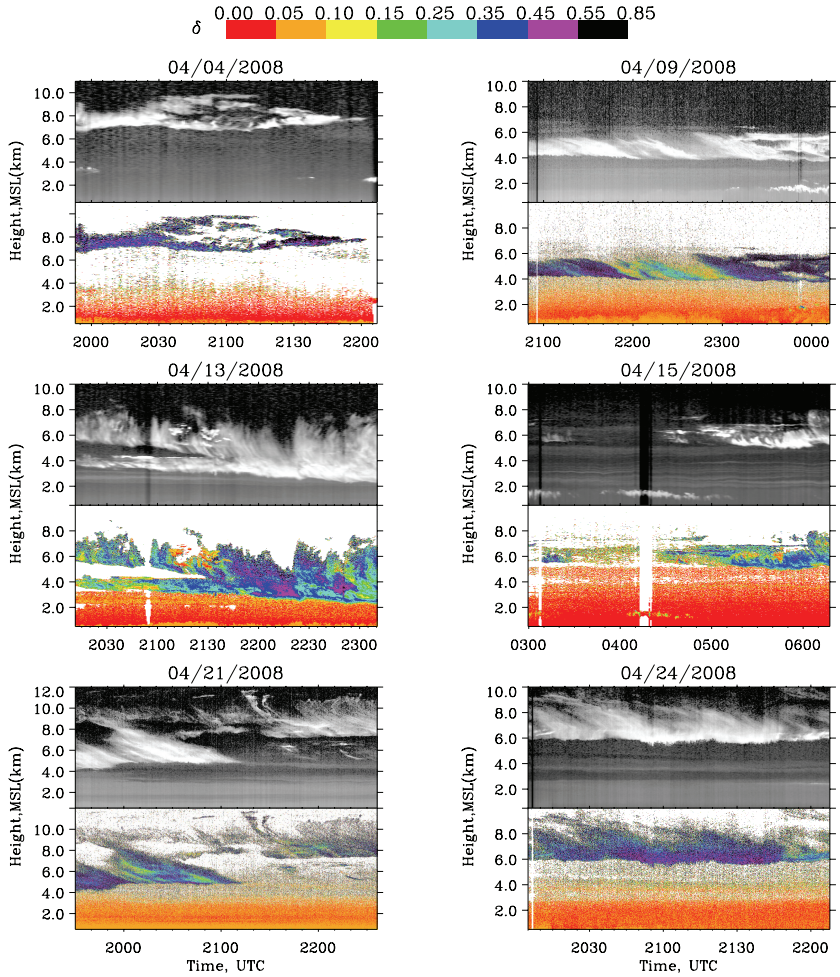

Fig. 2. Lidar results panel of 6 plots: **(a)** 4 April; **(b)** 9 April; **(c)** 13 April; **(d)** 15 April; **(e)** 21 April; **(f)** 24 April.

ACPD
11, 16499–16552, 2011

ARCTAS-A ground-based observational campaign, Alaska

D. E. Atkinson et al.

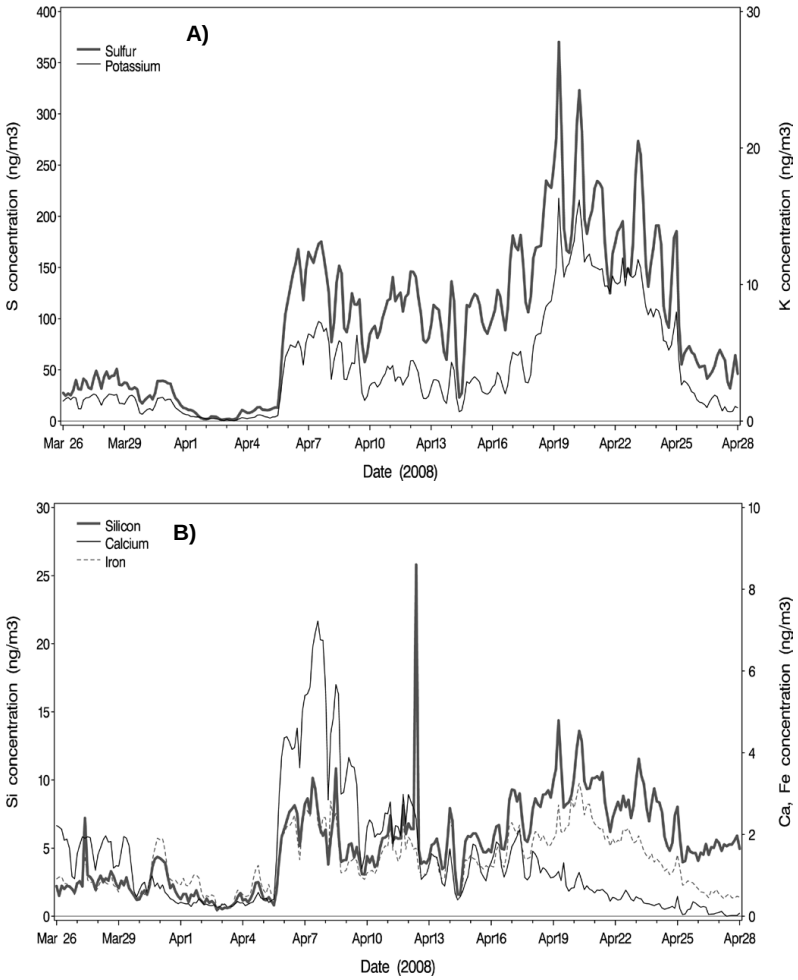

Fig. 3. Drum sampler species traces: **(A)** wildfire species (S, K); **(B)** mineral species (Fe, Si, Ca).

ACPD
11, 16499–16552, 2011

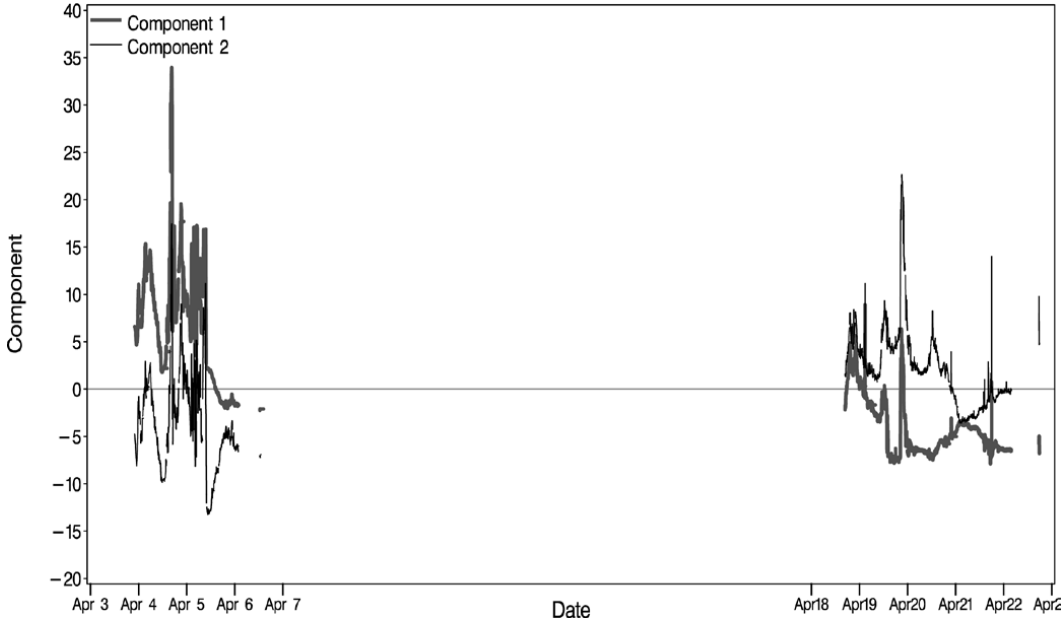

Fig. 4. Time series of component scores one and two from a principal components analysis conducted on the data from the Scanning Mobility Particle Spectrometer (SMPS) instrument.

ACPD
11, 16499–16552, 2011

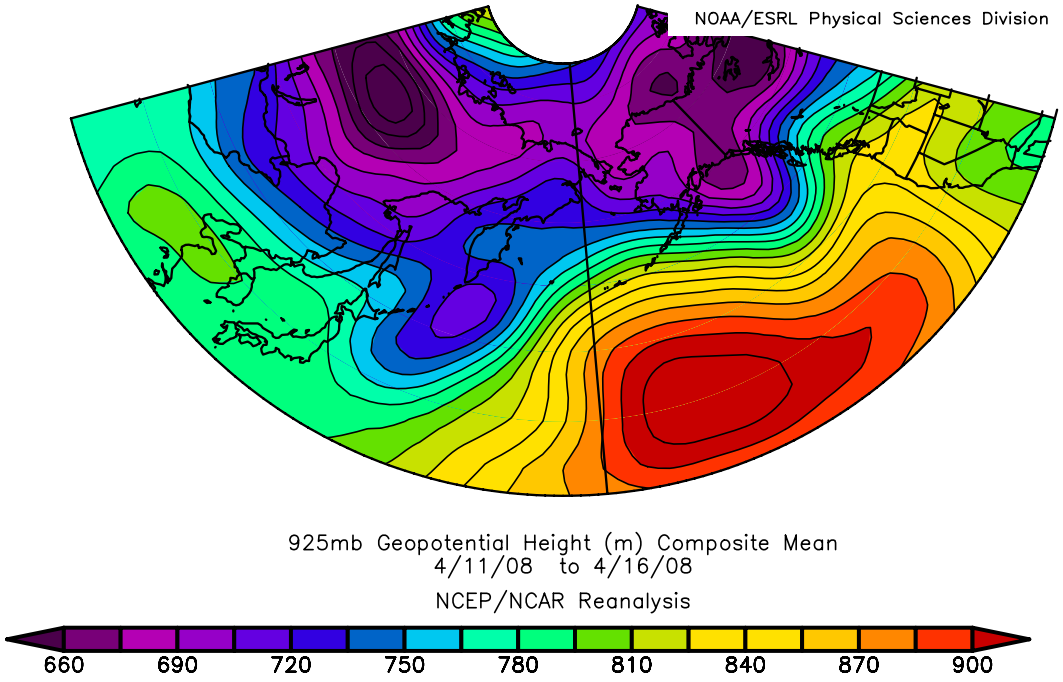

Fig. 5. Pressure at 925 mb for 11–16 April. The large high pressure zone south of the Aleutians pushes the Asian exit flow northwards such that it is in a position to move into the AK Interior between the mountain ranges. This represents the most favorable pathway to transfer unmodified airmasses into the Interior. This period captures the general trajectory leading to the balloonsonde launch of 19 April.

ACPD
11, 16499–16552, 2011

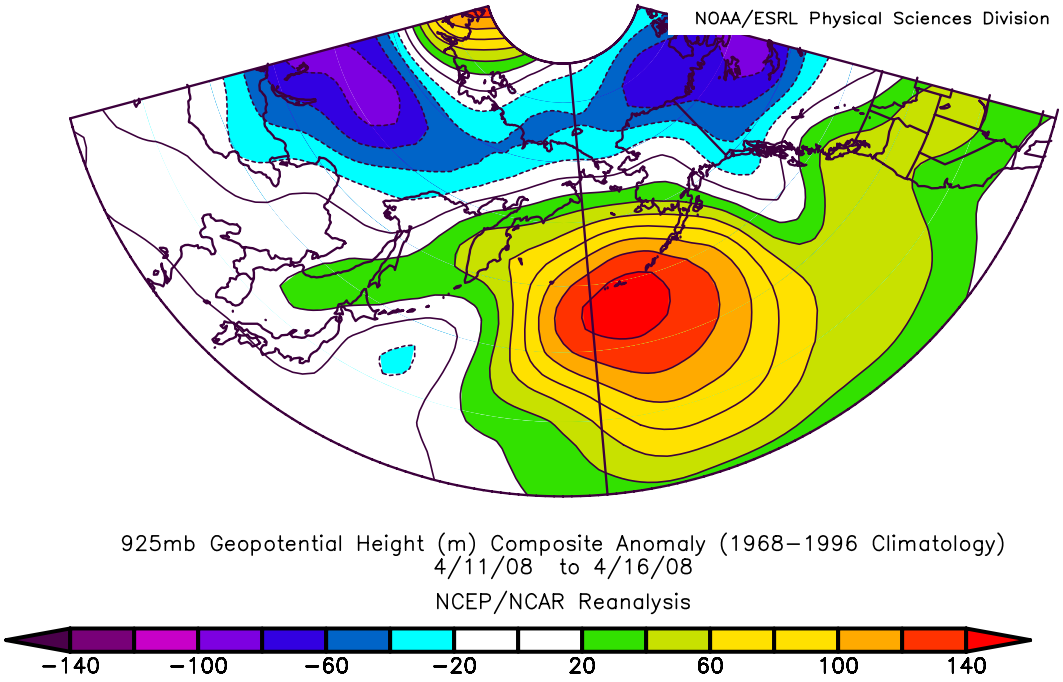

Fig. 6. Anomaly for the same date and parameter as shown in Fig. 5. The region of high pressure over the Aleutians during this period is not typical for this period.

ACPD
11, 16499–16552, 2011

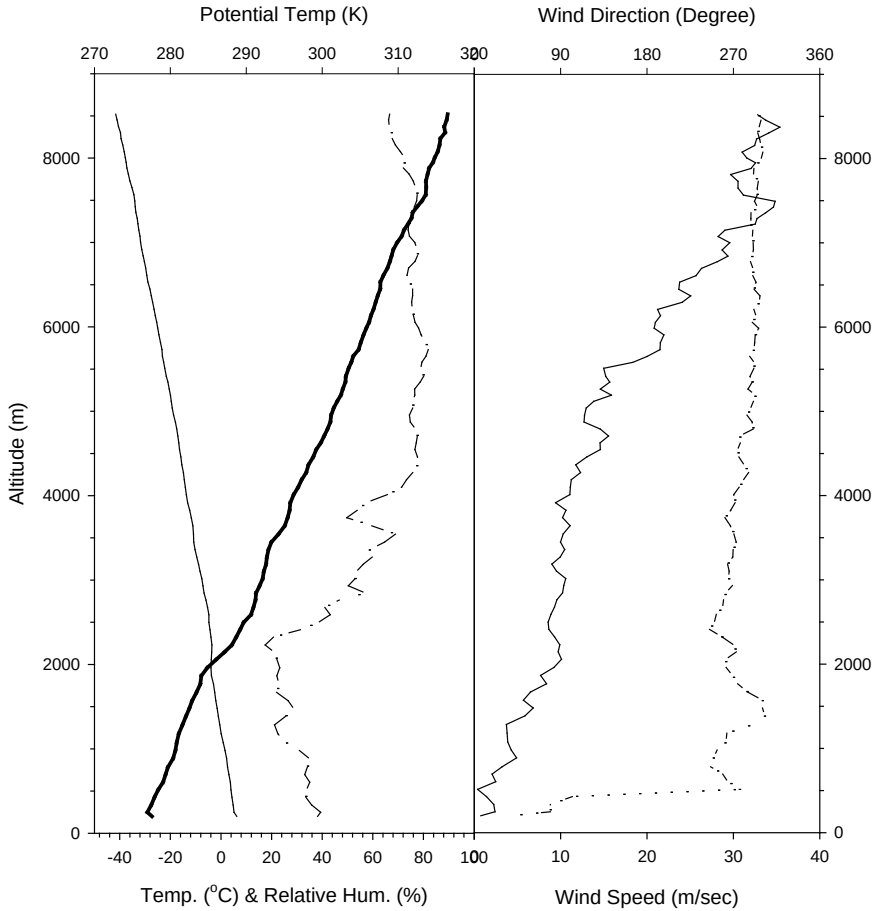

Fig. 7. Vertical profiles of meteorological parameters measured by the OPC sonde, 19 April 2008. **(a)** Temperature (thin line), potential temperature (heavy line), and humidity (dashed line), and **(b)** wind speed (solid line) and direction (dashed line) profiles observed with meteorological sonde.

ACPD
11, 16499–16552, 2011

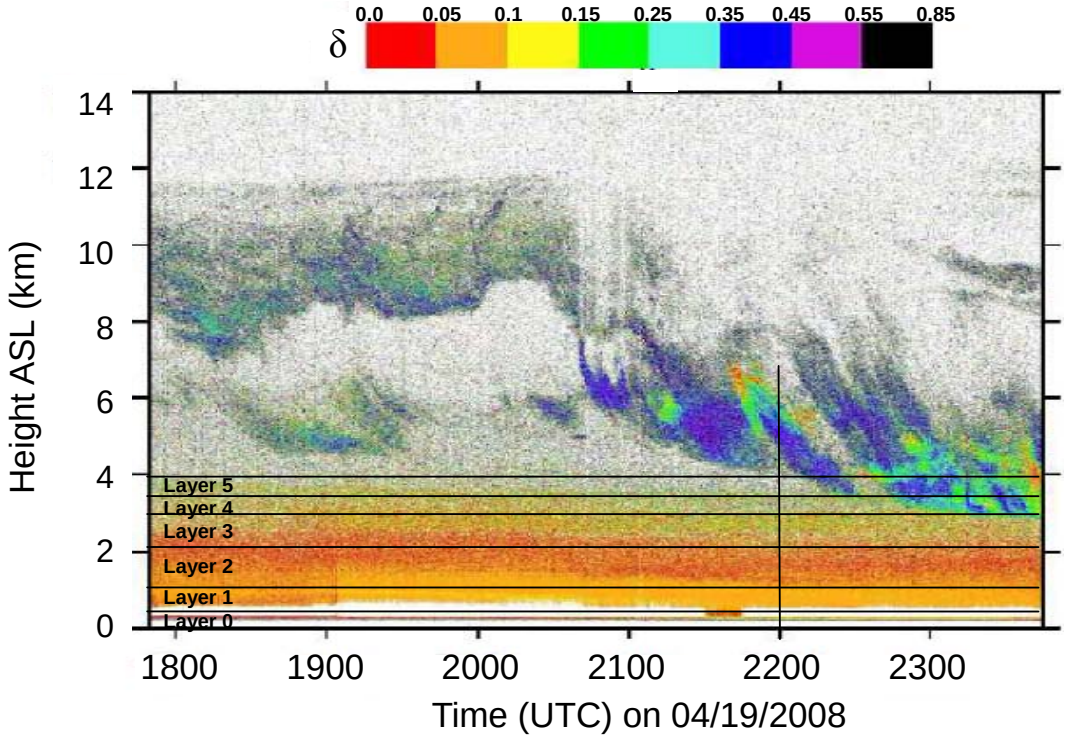

Fig. 8. Lidar depolarization ratio. Layers defined in the text are marked and labeled.

ACPD
11, 16499–16552, 2011

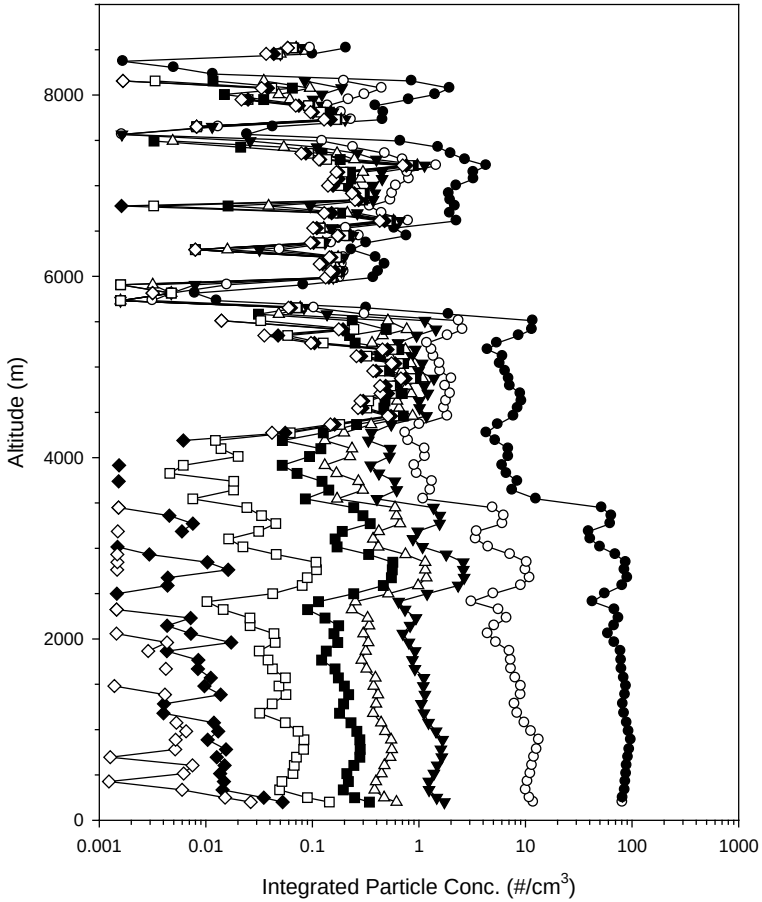

Fig. 9. Vertical profiles of aerosol concentrations observed with the OPC sonde. Horizontal axis represents integrated counts of particles, expressed as unit concentrations, arranged by size fraction. The size fractions represented are listed on the figure legend.

ACPD
11, 16499–16552, 2011

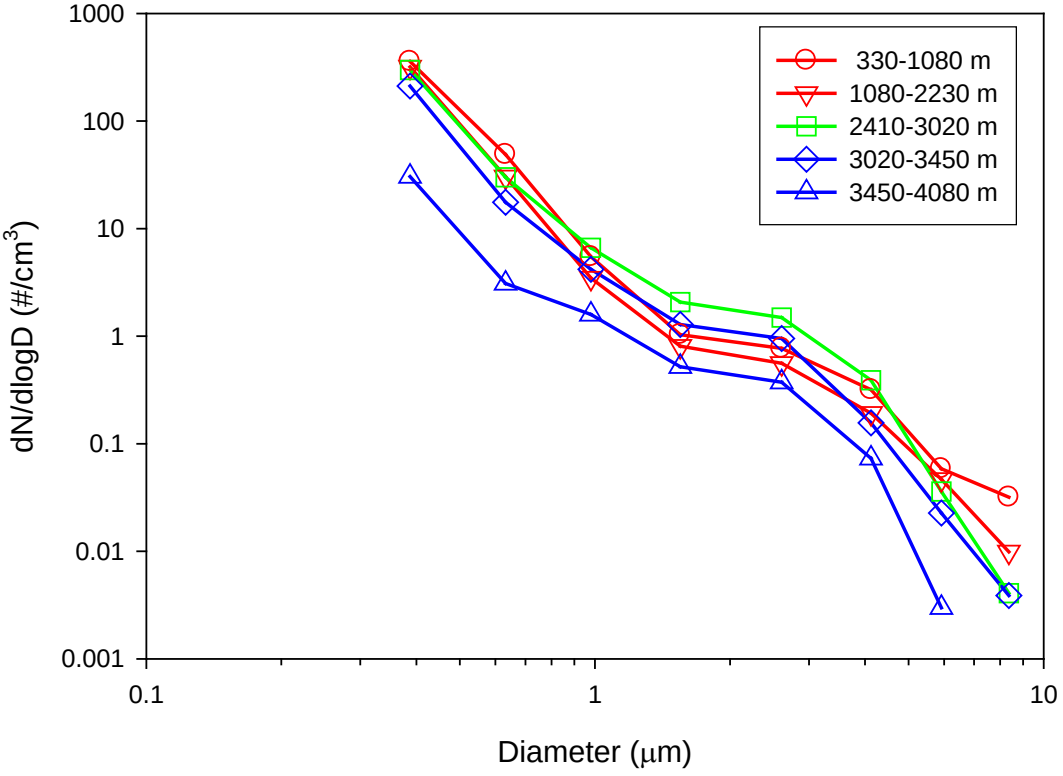

Fig. 10. Number size distributions in classified layers below 4.1 km.

ACPD
11, 16499–16552, 2011

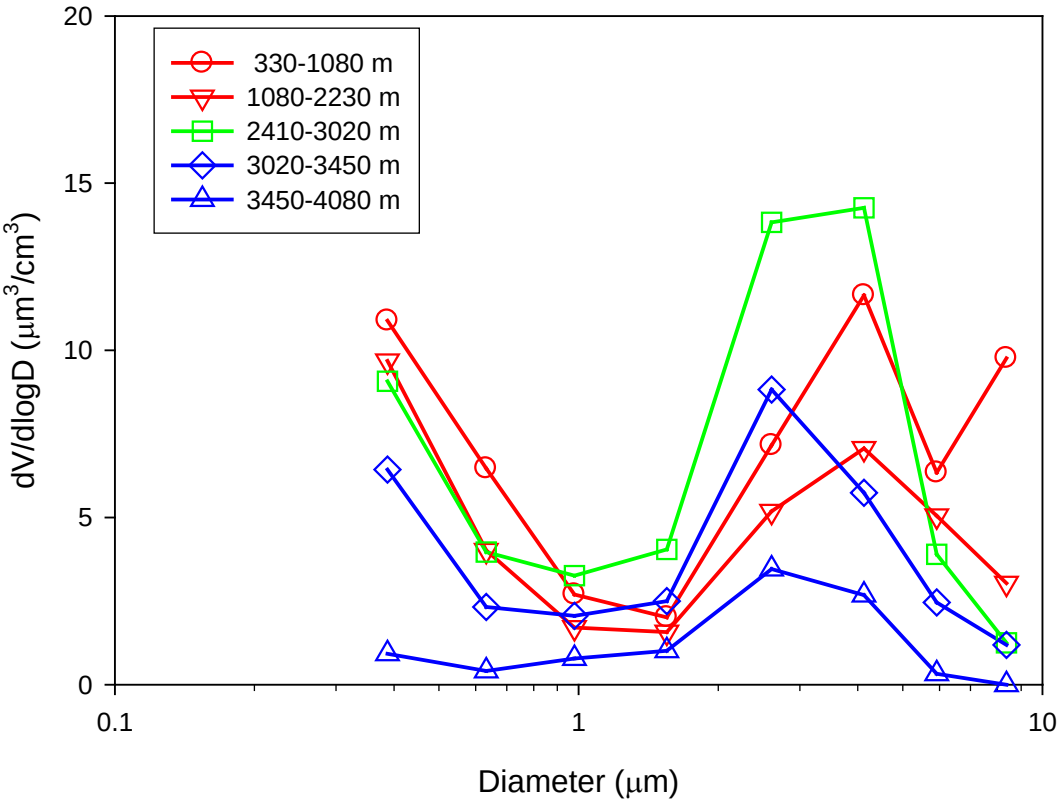

Fig. 11. Volume size distributions in classified layers below 4.1 km.

ACPD
11, 16499–16552, 2011

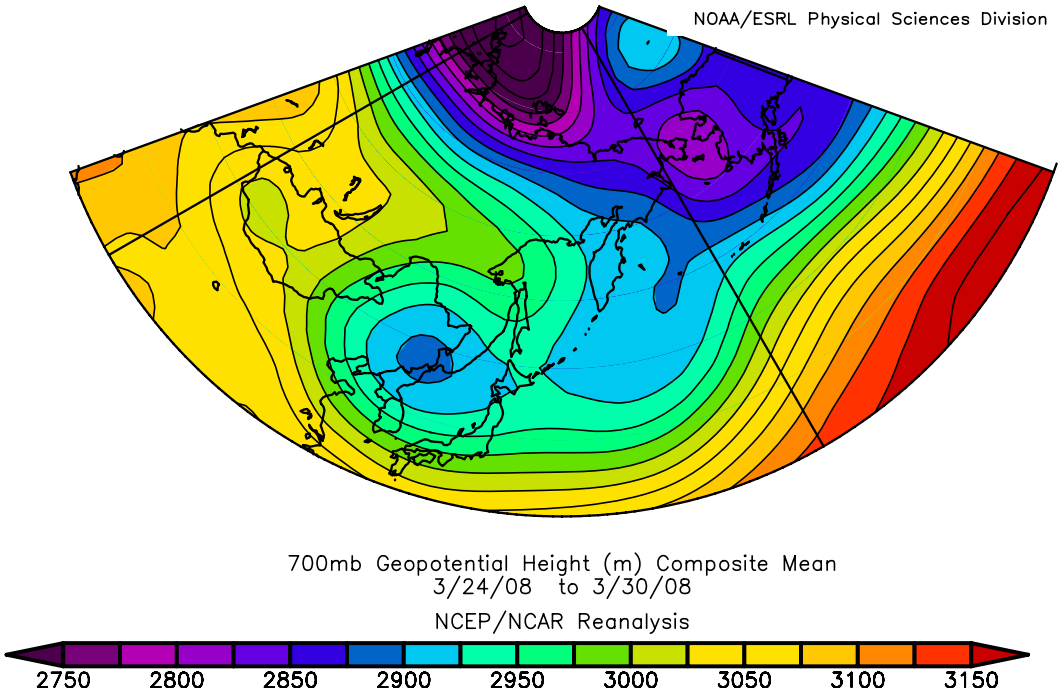

Fig. 12. Synoptic situation, 24–30 March 2008. 700 mb GPZ (m).

ACPD
11, 16499–16552, 2011

ARCTAS-A ground-based observational campaign, Alaska

D. E. Atkinson et al.

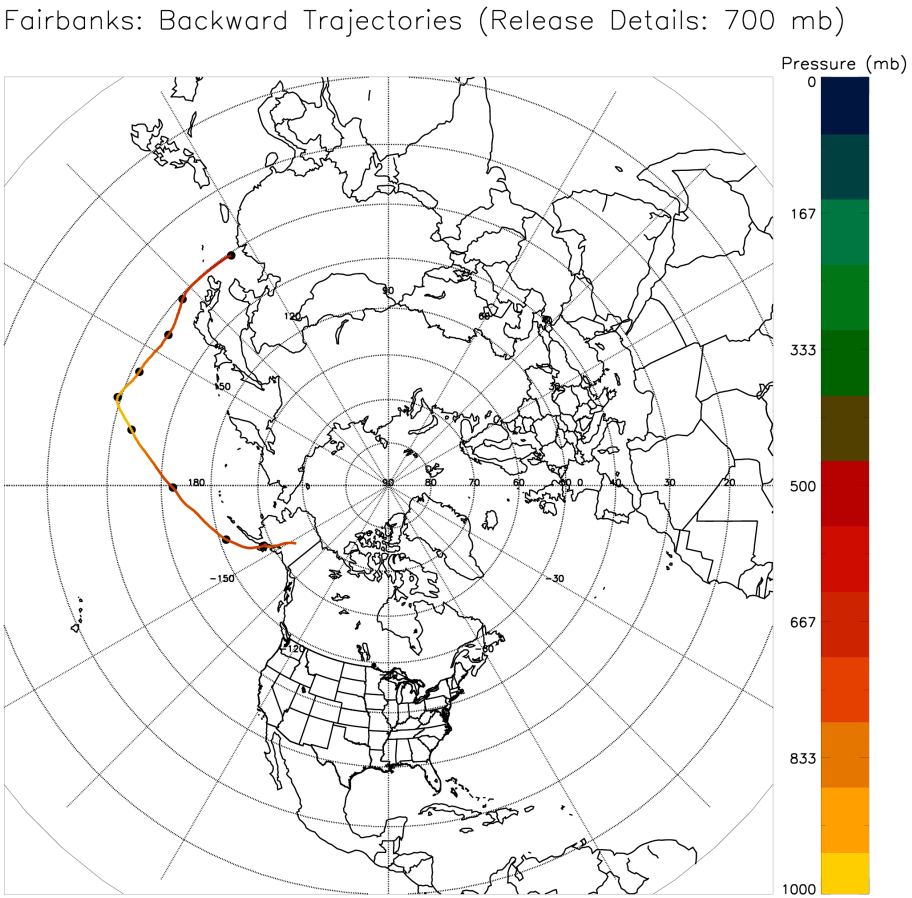

Fig. 13. FLEXPART back trajectory ending 3 April 2008 at 700 mb over Fairbanks, Alaska. Elevation for all FLEXPART trajectories was determined using distinct layers observed in the lidar data.

ACPD
11, 16499–16552, 2011

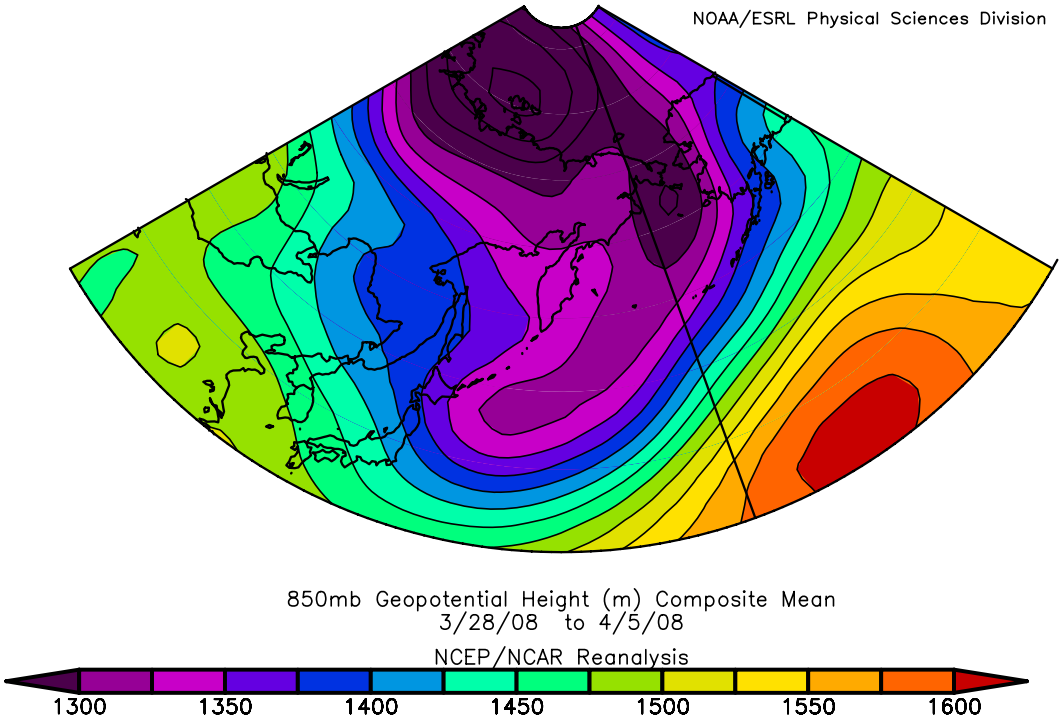

Fig. 14. Average synoptic situation, 28 March–5 April 2008. 850 mb GPZ (m).

ACPD
11, 16499–16552, 2011

ARCTAS-A ground-based observational campaign, Alaska

D. E. Atkinson et al.

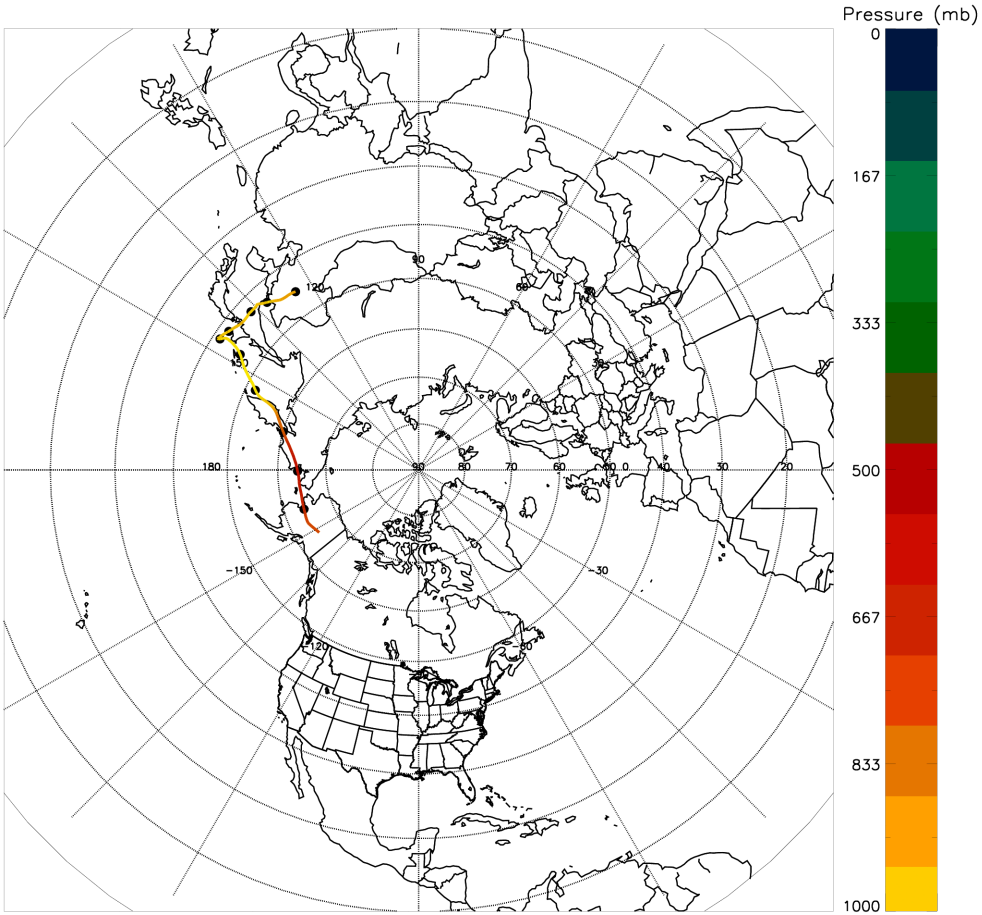

Fig. 15. FLEXPART back trajectory ending 13 April 2008 at 700 mb over Fairbanks, Alaska.

ACPD
11, 16499–16552, 2011

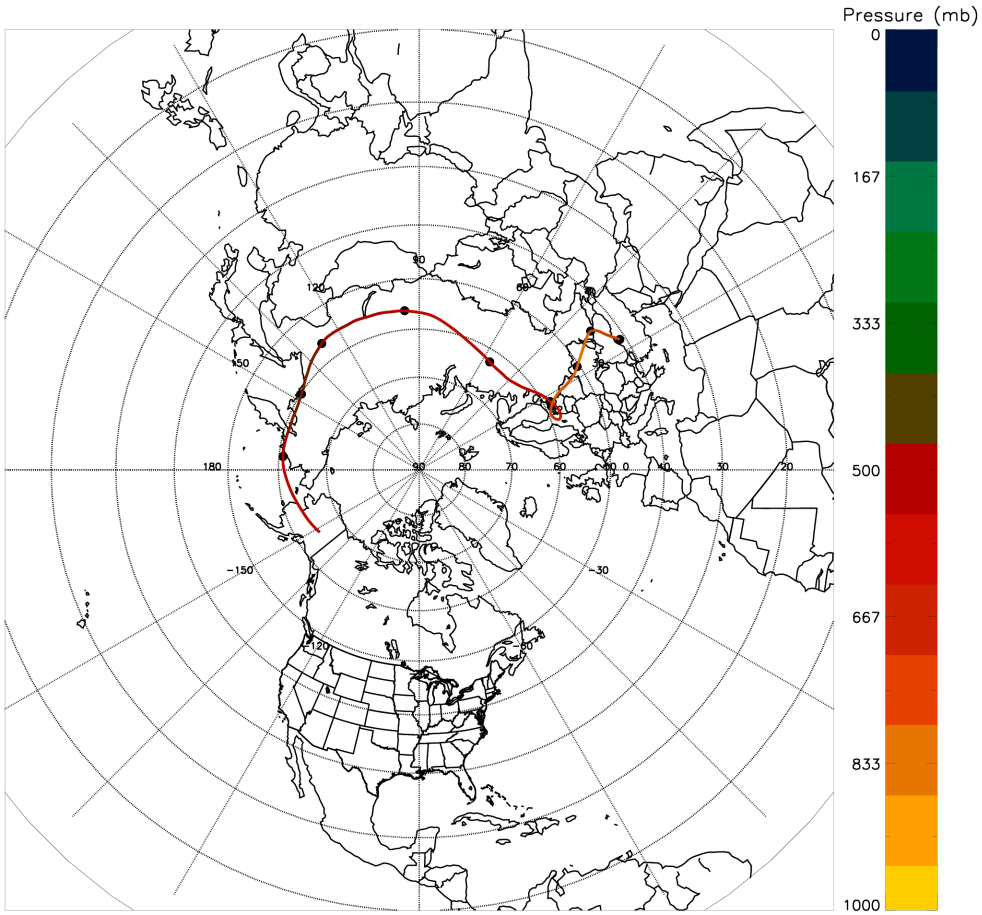

Fig. 16. FLEXPART back trajectory ending 15 April 2008 at 520 mb over Fairbanks, Alaska.

ACPD
11, 16499–16552, 2011

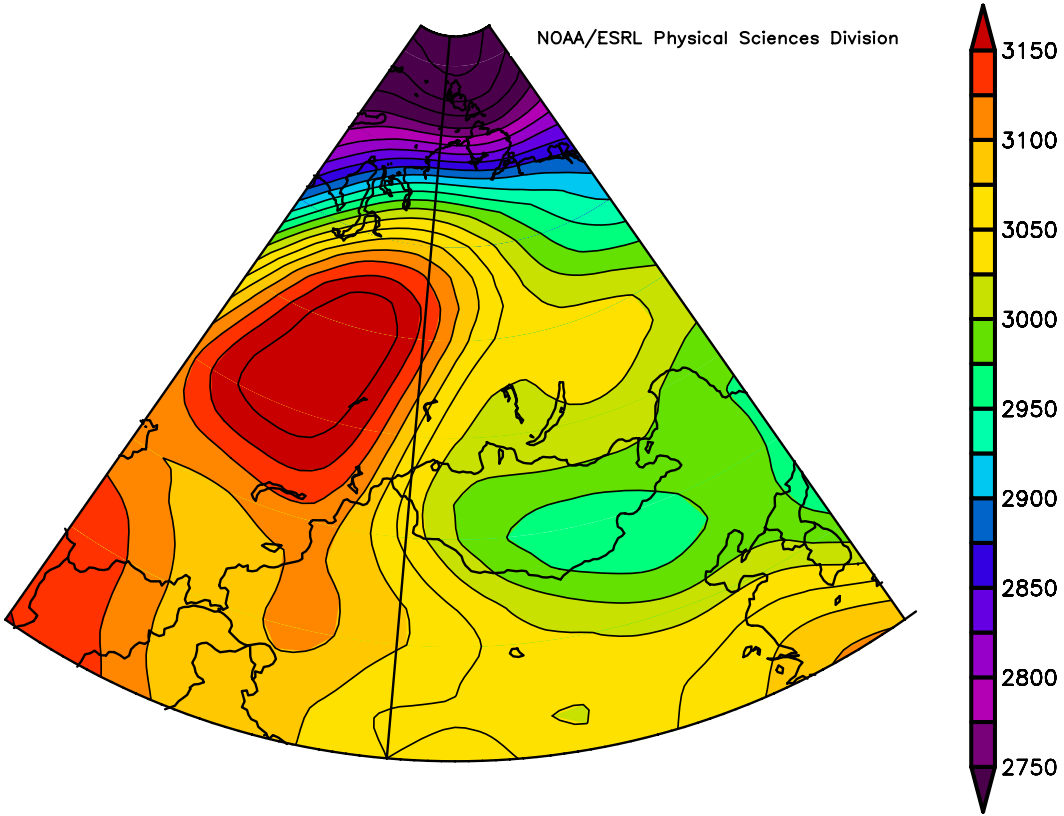

Fig. 17. Synoptic situation, 28 March 2008. 700 mb GPZ (m). Possible Takla Makan dust-raising event.

ACPD
11, 16499–16552, 2011

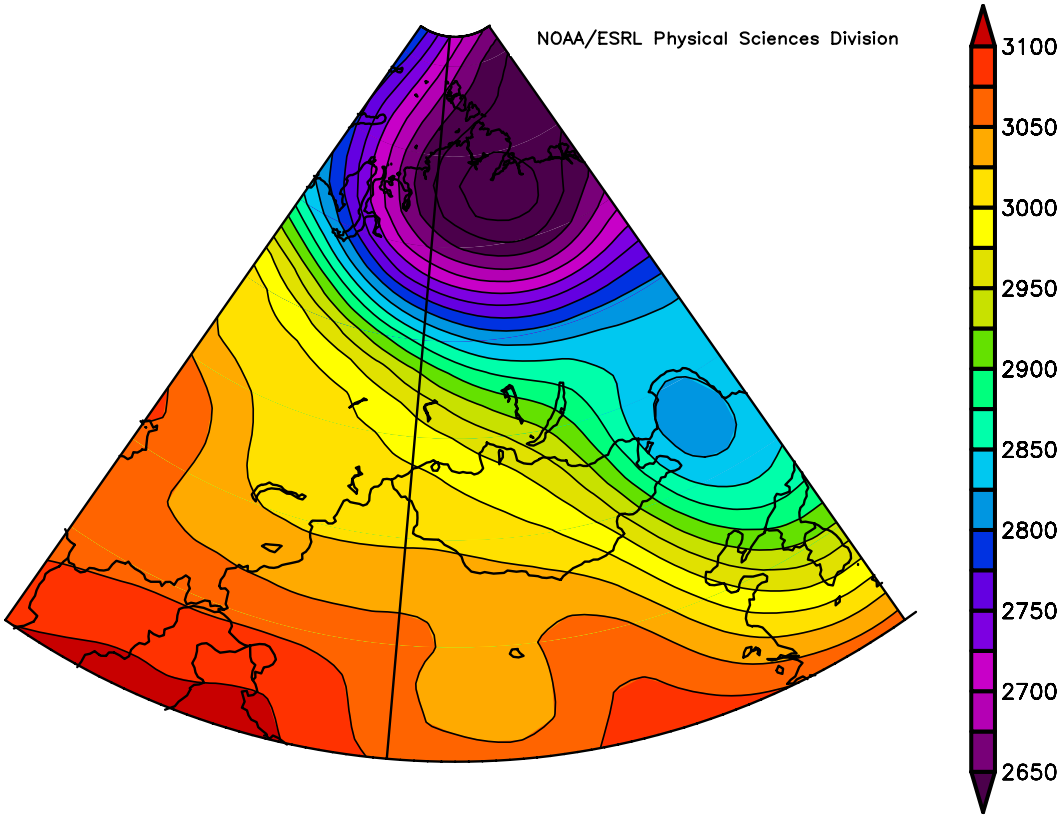

Fig. 18. Synoptic situation, 2 April 2008. 700 mb GPZ (m). Possible Gobi dust raising event.

ACPD
11, 16499–16552, 2011

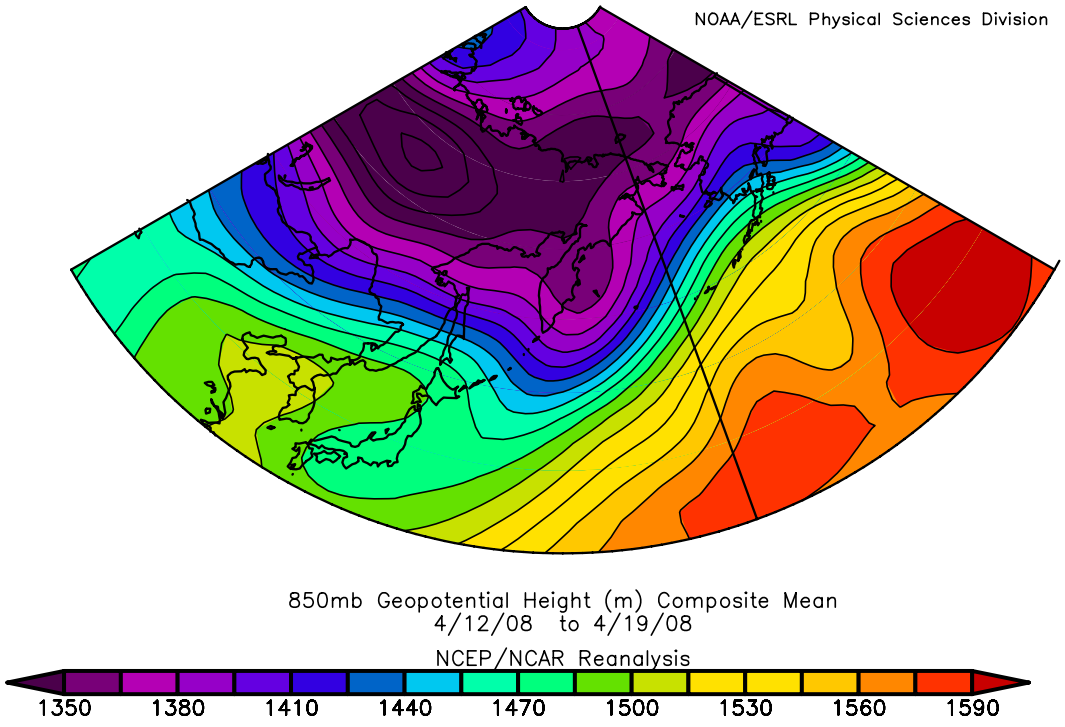

Fig. 19. Synoptic situation, 12–19 April 2008. 850 mb GPZ (m).

ACPD
11, 16499–16552, 2011

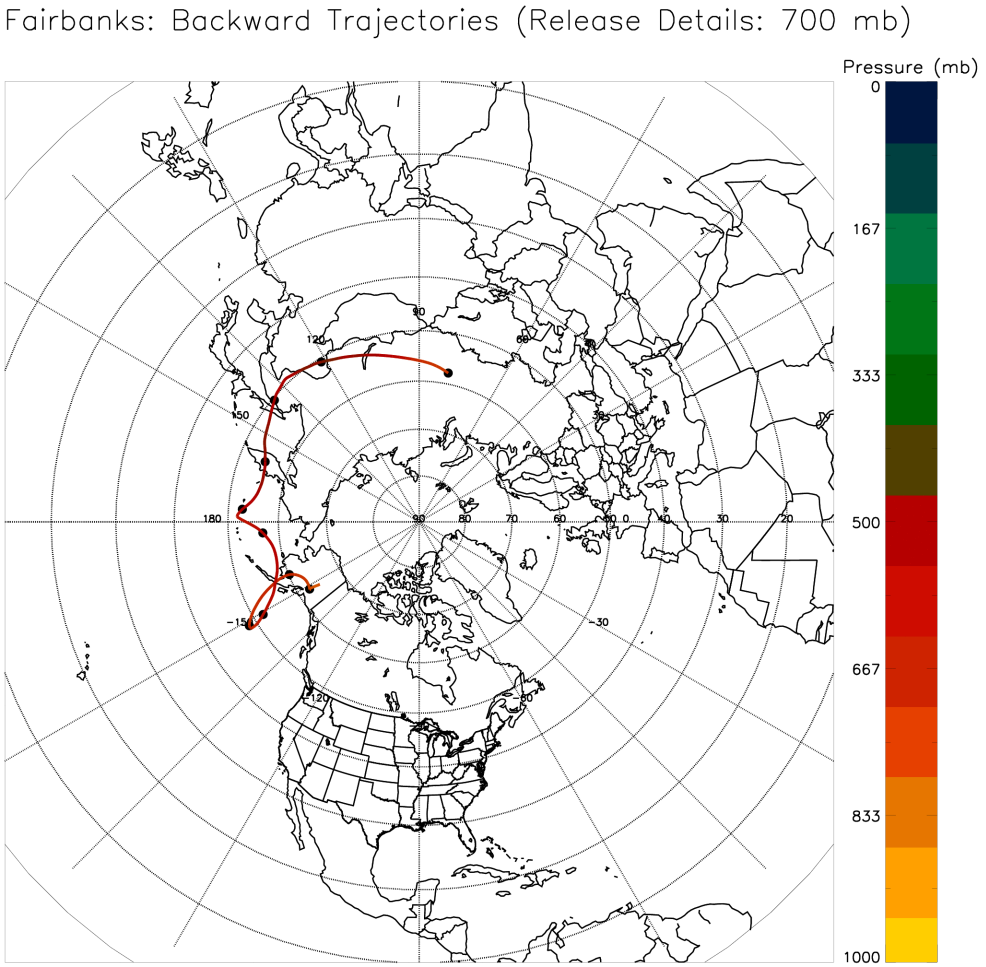

Fig. 20. FLEXPART back trajectory ending 21 April 2008 at 700 mb over Fairbanks, Alaska.

ACPD
11, 16499–16552, 2011

ARCTAS-A ground-based observational campaign, Alaska

D. E. Atkinson et al.

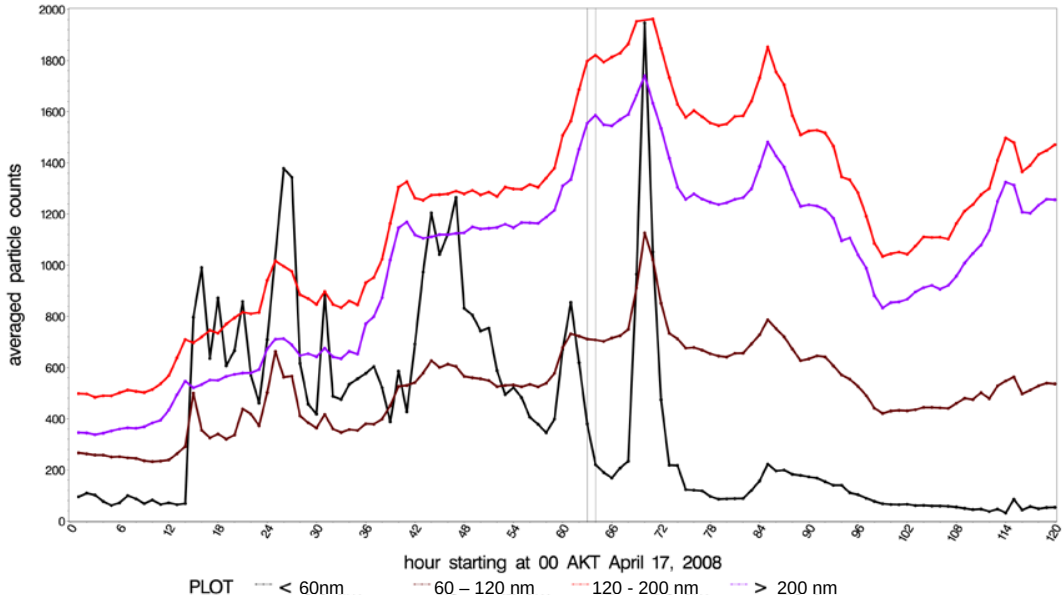

Fig. 21. Averaged traces from the Scanning Mobility Particle Spectrometer (SMPS) based north of Fairbanks. Data are shown for the five days surrounding the OPC sonde launch (OPC sonde timeframe indicated with vertical lines).

ACPD
11, 16499–16552, 2011

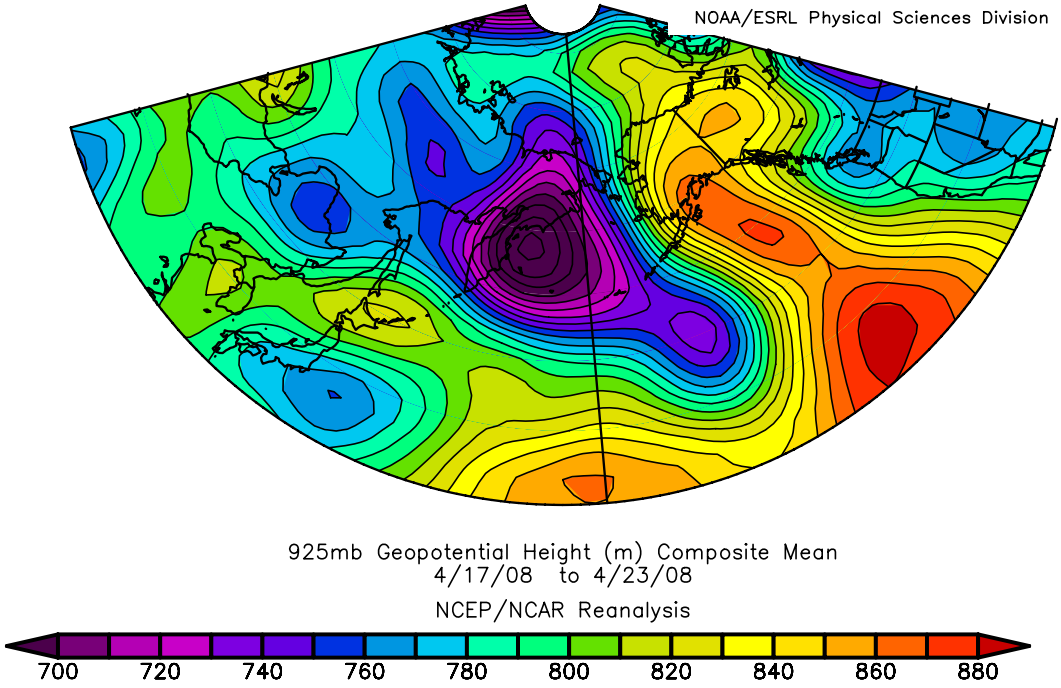

Fig. 22. Mean gpz for 17–23 April at 925 mb GPZ (m). This period was dominated by the incursion of a large low pressure system from the west into the Bering Sea. The anomalous high was displaced to the east. The resulting strong flow from the south brought a pronounced warming trend to the Interior. As the low moved in it displaced the main trajectory progressively farther to the south, increasing transport distance and showing up as a steady decrease in wildfire species into late April.

ACPD
11, 16499–16552, 2011